City Research Online

City St George's, University of London

Citation: Salah, S. I., Abdeldayem, A. S., White, M. & Sayma, A. I. (2024). Off-design performance assessment of an axial turbine for a 100 MWe concentrated solar power plant operating with CO2 mixtures. Applied Thermal Engineering, 238, 122001. doi: 10.1016/j.applthermaleng.2023.122001

Permanent repository link: https://openaccess.city.ac.uk/id/eprint/31759/

Link to published version: https://doi.org/10.1016/j.applthermaleng.2023.122001

Applied Thermal Engineering 238 (2024) 122001

Contents lists available at ScienceDirect

Applied Thermal Engineering

journal homepage: www.elsevier.com/locate/ate

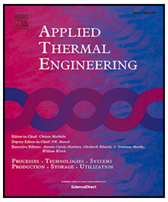

Research Paper

Off-design performance assessment of an axial turbine for a 100 MWe concentrated solar power plant operating with CO_2 mixtures

Salma I. Salah [a,b,*], Abdelrahman S. Abdeldayem [a], Martin T. White [a,c], Abdulnaser I. Sayma [a]

[a] Energy, Sustainability and Net Zero Research Centre, City, University of London, Northampton Square, London, EC1V 0HB, United Kingdom
[b] Department of Mechanical Engineering, The British University in Egypt (BUE), El Sherouk City, Cairo, 11837, Egypt
[c] Thermo-Fluid Mechanics Research Centre, School of Engineering and Informatics, University of Sussex, Brighton BN1 9RH, United Kingdom

ARTICLE INFO

Keywords:
sCO_2 turbines
CO_2 mixtures
Axial turbines
Off-design performance
Similitude theory
Mean-line model
CFD simulations

ABSTRACT

This paper presents an investigation of the aerodynamic performance of a 130 MW axial turbine operating with a CO_2/SO_2 mixture using a mean-line off-design performance model; where the validity of this model has been confirmed through verification against results from the literature and computational fluid dynamic (CFD) simulations. This analysis also includes assessing the impact of varying the number of stages on the part-load operation. Additionally, the application of similitude theory to non-dimensionalise performance characteristics is validated by assessing the performance of the same turbine with different working fluids, mixture compositions, and rotational speeds. The mean-line performance model applied throughout this study is based on the Aungier loss model, whilst a multi-stage, Reynolds averaged CFD model is employed to assess the 3D flow behaviour using the $k-\omega\ SST$ turbulence model. Significant deviations in total-to-total efficiency were observed between the mean-line and CFD results during part-load operation, especially at lower mass flow rates. These deviations can reach up to 18% when the blade Mach number exceeds the design point by 12%. This is attributed to flow separation, which is evident from the CFD simulations, and the mean-line loss model fails to predict. From a purely aerodynamic standpoint, the turbine can operate at part-load conditions up to 88.5% of the design flow coefficient based on the CFD results and achieve an efficiency of 80.2%. It was also found that increasing the number of stages from 4 to 14 can improve the off-design total-to-total efficiency by approximately 7.7% at 93% of the design flow coefficient. This demonstrates that increasing the number of stages enhances turbine performance at both design and part-load operations. Finally, the similitude scaling laws formulated using real-gas equation of state were found to remain valid for all the mixtures, molar compositions, and operating conditions considered.

1. Introduction

The utilisation of CO_2 mixtures in power cycles can bring advantages to concentrated solar power (CSP) applications, leading to improved performance of the power block that could ultimately reduce the Levelised Cost of Energy (LCoE) of the technology. Adopting CO_2 mixtures instead of pure sCO_2 can increase the critical point of the working fluid, allowing for condensation at elevated cooling medium temperatures. Therefore, in the case of CSP applications where cooling water is not readily available, condensation can be achieved using ambient air which results in a substantial reduction in the compression work required to generate the same output.

The European Commission funded SCARABEUS project [1] aims to demonstrate the potential of using CO_2 mixtures for large-scale plants in the order of 100 MW_e. To date, multiple mixtures have been identified as being particularly promising, namely titanium tetrachloride ($TiCl_4$) [2], hexafluorobenzene (C_6F_6) [3] and sulphur dioxide (SO_2) [4]. These mixtures have demonstrated a significant potential in enhancing the thermal efficiency of the cycle while implementing simple cycle configurations such as simple recuperation for $TiCl_4$, precompression for C_6F_6, and recompression for SO_2. It is important to note that the thermal stability and environmental considerations of these mixtures have been investigated within the SCARABEUS project. The results of these investigations indicated that out of the three mixtures, only the CO_2/C_6F_6 mixture shows signs of thermal degradation at temperatures above 600 °C [5]. Furthermore, none of the selected mixtures exhibits significant global warming potential or ozone depletion potential.

---

* Corresponding author.
E-mail address: salma.salah.2@city.ac.uk (S.I. Salah).

https://doi.org/10.1016/j.applthermaleng.2023.122001
Received 26 July 2023; Received in revised form 9 October 2023; Accepted 12 November 2023

Nomenclature

A

CFD	computational fluid dynamics
CSP	Concentrated Solar Power
LCoE	Levelised cost of energy
ML	Mean-line
PR	Pressure ratio
TES	thermal energy storage (TES)

G

α	Enthalpy loss coefficients
β	Enthalpy loss coefficients
Δ	Diffusion angles
η_{tt}	Total-to-total efficiency [%]
γ	Stagger angles
μ	Viscosity
Φ_m	Flow coefficient
ρ	Density
ζ	Enthalpy loss coefficients

R

A	blade areas [m]
C	Absolute velocity
c	Chord length [m]
C_a	Axial velocity
D	Diameter [m]
h	Blade heights [m]
I	Rothalpy
i	Incidence
l	Length
Ma_b	Blade Mach number
n	The number of blades
P	Static pressure
P_0	Total pressure
R	Radius [m]
R	Rotational speed
s	Blade pitch [m]
ss	Axial spacing [m]
T	Static temperature
T_0	Total temperature
U	Blade speed [m/s]
w	Relative velocity
X_i	Fluid molar fraction

S

1	Stator inlet
2	Rotor inlet
3	Rotor outlet
d	at the design point
hub	at the hub
R	Rotor
S	Stator

The performance of CSP power cycles is significantly affected by the variable nature of solar irradiation, which can fluctuate due to seasonal and weather changes. These changes result in part-load operating conditions, which can further affect the system's overall performance. Therefore, the integration of efficient and cost-effective thermal energy storage (TES) systems is a crucial element in the advancement of concentrated solar power (CSP) technology. The role of TES systems extends beyond bridging the gap between energy supply and demand. These systems enhance the performance and reliability of energy systems, while also playing a vital role in energy conservation [6].

The accuracy of the cycle performance predictions is significantly dependent on the accuracy of the part-load performance models of the different cycle components, which includes the turbine as a critical component. During turbine aerodynamic design the main objective is typically to optimise efficiency at the design point, where the blade angles are designed to match the direction of the flow. Throughout this process, different types of aerodynamic losses are evaluated, which includes profile losses, secondary flow losses, tip clearance losses, trailing edge losses, and potentially shock and supersonic expansion losses. However, turbines frequently operate under part-load conditions where the flow can deviate from the design operating conditions, and this is particularly true during turn-down when a lower power output is needed. In these operational scenarios, there is the possibility of a mismatch between the flow angle and the blade angle, which occurs as a result of the decrease in mass flow rates. The mismatch between the inlet flow angle can result in regions of recirculation, which leads to aerodynamic loss referred to as incidence losses. During the mean-line design process, incidence losses are typically evaluated using empirical loss models. However, these models are not specifically calibrated for turbines operating with supercritical carbon dioxide (sCO_2) and CO_2 mixtures at part-load operation, which leads to the uncertainty of their accuracy. Consequently, it is important to thoroughly investigate the suitability of these models to accurately predict the performance of turbine operating with CO_2 mixtures for concentrated solar power (CSP) applications across a wide range of expected operating conditions.

Performance maps are used to characterise the off-design performance of turbines. These maps report the relationship between turbine performance, defined in terms of total-to-total or total-to-static efficiency and pressure ratio, across a range of mass flow rates at multiple rotational speeds. Principally, performance maps should be generated using test data. However, in the absence of suitable experimental data or test rigs, mean-line tools and computational fluid dynamic (CFD) simulations can be used to create these maps. In particular, there have been several test rigs developed for sCO_2 turbines, including prototypes with power outputs up to 8 MW [7–12]. However, among these prototypes, only one is a 1 MW axial turbine, while the rest are of radial turbine configuration. The limited number of prototypes, alongside the substantial costs associated with constructing test facilities, makes it challenging to validate designs and generate performance maps using experimental data. Moreover, the complexity of carrying out tests means only a limited number of operating conditions can typically be tested, and the resulting dimensional maps can be of limited use when analysing turbine performance within cycle analysis. Consequently, similitude theory becomes essential in order to non-dimensionalise the performance map and widen its range of applicability in cycle analysis.

Performance maps are generated using non-dimensional groups defined using formulations designed for both ideal and real gases. These maps rely on three main non-dimensional groups: the flow coefficient, head coefficient, and blade Mach number. When the working fluid behaviour deviates from the ideal gas law, these non-dimensional groups are expressed for real gases, incorporating functions of the mass flow rate, inlet speed of sound, isentropic enthalpy drop, inlet density, diameter, and rotational speed to accurately represent the system's performance. The use of the isentropic relationship for perfect gases results in ideal gas formulations that are expressed in terms of the pressure ratio, reduced mass flow rates, and reduced speeds. These formulations are functions of the pressure ratio, mass flow rate, inlet temperature, gas constant, specific heat ratio, and diameter.

Similitude theory has been widely applied for turbines operating with ideal gases such as air [13–15]. Moreover, several studies have employed the similitude theory to model the off-design performance of turbines that operate with non-conventional working fluids, including CO_2 and other organic working fluids which may not obey the ideal-gas law in the proximity of the saturation dome. Zhang et al. [16] applied similitude theory to a radial turbine operating with organic working fluids where the turbine performance was predicted using CFD simulations; the turbine performance maps were non-dimensionalised using ideal-gas formulations. Zhou et al. [17] investigated the off-design performance of a radial inflow sCO_2 turbine using both one-dimensional model and 3D CFD simulations. The off-design maps were presented using the ideal gas form of the similitude scaling rules. Finally, Peng et al. [18] investigated the off-design performance analysis for ORC and CO_2 turbines using a mean-line performance model. The performance maps were generated using maps that were non-dimensionalised using ideal-gas formulations. On the contrary, the validity of similitude theory to ORC turbines has also been previously investigated by some of the current authors. More specifically, White & Sayma [19] formulated the non-dimensional groups using density and speed of sounds values calculated directly using a real-gas equation of state. The performance predictions obtained using the non-dimensional maps for a small-scale radial turbine were compared to CFD simulation results. According to the analysis, it was concluded that real-gas non-dimensional maps formulated using the total inlet conditions were only applicable to a narrow range of operating conditions where the flow is subsonic. A modified similitude formulation was suggested based on the choked flow conditions. A good agreement was achieved between the modified theory and the CFD results with a difference of 2%.

Among the previous studies, several researchers have evaluated the off-design performance of turbines using the existing mean-line loss models. These evaluations were conducted for turbines operating with non-conventional working fluids such as CO_2 and other organic fluids. Hu et al. [20] analysed the off-design performance using mean-line loss models for a radial turbine operating with an organic working fluid to predict the off-design losses. Similarly, Zhou et al. [17] predicted the turbine off-design performance using a 1D dimensional model, and the off-design predictions of the mean-line model were consistent with the numerical CFD solutions in the working range of the sCO_2 radial inflow turbine, with a maximum deviation of 5% between the mean-line model and numerical solution. Ultimately, Peng et al. [18] investigated the off-design performance analysis for ORC and CO_2 turbines using a mean-line performance model integrated with the Aungier loss model.

Based on the presented review, it can be deduced that both real gas and ideal gas formulations have been utilised to generate performance maps for turbines operating with non-conventional working fluids such as pure CO_2 and other organic fluids. Furthermore, it is evident that none of the previous studies has investigated the validity of similitude theory in the context of turbines operating with different CO_2 mixtures. As a result, further exploration and investigation are required to determine the most suitable approach for dealing with CO_2 mixtures and to establish the validity of similitude theory for CO_2 mixtures.

Furthermore, while some studies have used mean-line loss models to evaluate the off-design performance of turbines operating with CO_2 and other organic working fluids, none of the previous studies has specifically examined the predictive capability of mean-line loss models for assessing the off-design performance of axial turbines designed with a large number of stages that operate with CO_2 mixtures.

The aim of this paper is to investigate the off-design performance of large-scale multi-stage turbines operating with CO_2 mixtures using both mean-line and CFD models. Additionally, the paper aims to evaluate the validity of existing mean-line off-design loss models in predicting the performance of turbines operating with CO_2 mixtures and investigate the applicability of similitude theory for turbine scaling. This is done with a view to evaluating the suitability of existing mean-line off-design loss models, and similitude theory, for turbines operating with CO_2 mixtures. This includes investigating the impact of the number of stages on the off-design performance and analysing the discrepancies between the CFD simulations and the mean-line model across all the turbine stages. The novelty of this work lies in comparing the mean-line performance predictions with the results from CFD simulations for CO_2 mixtures under various off-design operating conditions. This comparison involves analysing the power distribution and performance metrics, such as total-to-total efficiency and loss coefficients per stage, and assessing the cumulative effect of flow incidence in a multi-stage axial turbine. Furthermore, the study investigates the three-dimensional flow within each stage, and attempts to identify flow separation regions and correlate this with performance predictions. The results of this analysis offer the first insights into the off-design performance of axial turbines operating with CO_2 mixtures, whilst assessing the suitability of off-design loss models developed for air and steam turbines for non-conventional working fluids like CO_2 mixtures. The results from this study also determine whether similitude theory can be used to estimate turbine performance when different CO_2 mixtures, molar compositions, and operating conditions are considered.

The paper is structured as follows: Section 2 provides a summary of the off-design performance modelling methodology, covering the details of both the mean-line and CFD models. The verification of the methodology is discussed in Section 3. The results are presented and discussed in Section 4, including analysis concerning the flow path performance maps, the capability of the mean-line models, the three-dimensional flow characteristics, and the validity of similitude theory. Finally, Section 5 presents the main conclusions of this study.

2. Methodology of off-design performance analysis

The off-design performance analysis is conducted in this study using both a mean-line (ML) performance analysis approach and CFD simulations. Both methodologies are detailed in Section 2.1 & 2.2. The ML approach is capable of providing fast results with an acceptable level of accuracy, once suitably calibrated to the desired operating conditions. However, it should be noted that ML loss models may fall short in capturing 3D flow features, which can occur under off-design conditions and have a detrimental effect on turbine efficiency. On the other hand, CFD models simulate the 3D flow field rather than approximating the solution at the mean-line and thus provide a better understanding of the flow characteristics, leading to more accurate performance predictions. Nevertheless, the accuracy of CFD simulations highly depends on the modelling assumptions and the mesh quality that need to be assessed.

While the proposed methodology, utilising mean-line design and CFD tools, is widely applied in the literature, the application of these tools to turbines operating with CO_2 turbines at off-design operating conditions is limited. Furthermore, the large number of stages in this design, resulting from optimising the turbine efficiency, may impact the prediction capability of the mean-line loss models. Consequently, in the absence of experimental data, a comparison of ML and CFD results is conducted to quantify the deviations observed.

2.1. Mean-line model

To evaluate the turbine performance at off-design conditions, a mean-line performance approach has been adopted. For a given geometry, the off-design performance is evaluated at different operating conditions using the Aungier mean-line loss model. The model is first initialised by defining various turbine geometric parameters such as blade heights (h), chord length (c), stagger angle (ζ), blade speed (U), flow areas (A), blade angles (α' and β'), hub diameter (D_{hub}), and the number of blades (n_{blades}) as summarised in Table 1. Additionally, the off-design operating conditions need to be defined, which include specifying the mass flow rate ($\dot{m}$), total inlet pressure (P_{01}), total inlet temperature (T_{01}), and fluid molar fraction (X_i). Fluid properties are evaluated using the Peng Robinson equation of state using SIMULIS package [21], and the binary interaction parameters are obtained

Table 1
Input parameters for the off-design performance model.

Input geometry	Symbol	Input geometry	Symbol
Number of blades	n	Diffusion angles	Δ
Inlet/Outlet blade angles	α' & β'	Inlet/Outlet areas	A
Stagger angles	γ	Inlet/Outlet blade heights	h
Hub/tip radii	R_h & R_t	Blade pitch	s
Axial chord length	c	Clearance gap	t_{cl}
Axial spacing	ss	Blade peripheral speed	U
Throat-to-pitch ratio	o/s		

using values that are consistent with those derived during the cycle analysis [4,22]. Aqel et al. [23] investigated the effect of the equation of state on turbine design for three mixtures (i.e., CO_2/SO_2, $CO_2/TiCL_4$ and CO_2/C_6F_6) and found that the turbine designs for CO_2/SO_2 were the least sensitive to the fluid model. Overall, the maximum difference in turbine geometry was 6.3%, which corresponded to comparing the Soave-Redlich-Kwong and PC-SAFT equations of state. However, the differences were mainly due to variations in the boundary conditions imposed by the cycle analysis, rather than intrinsic variations within the expander.

At off-design operating conditions, a change in the turbine inlet mass flow rate will impact the axial velocity through the machine, which in turn alters the flow angles, leading to incidence losses and decreased turbine performance. To evaluate the turbine performance under off-design conditions accurately, it is crucial to consider various losses, including incidence losses, as well as profile, secondary flow, trailing edge, and tip clearance losses. The Aungier loss model [24] is employed to estimate the total aerodynamic losses in the flow path. To proceed with implementing this loss model here, it is worth noting here that the mean-line performance analysis is conducted at the mean diameter. It is assumed that, within any given cross-sectional plane between adjacent blade rows, the total pressure, total temperature, and axial velocity remain constant at all points. Although this assumption may deviate from the actual flow behaviour, it is expected to yield accurate overall characteristics of a stage if the flow angles and pressure loss coefficients used for each blade row at the reference diameter align with the momentum mean values across the entire cross-sectional plane, as determined through an actual flow investigation in the turbine. Hence, the accuracy of the performance calculation heavily relies on the ability to predict these mean loss coefficients and gas flow angles for each blade row. Having said that, it is worth highlighting that the Ainley and Mathieson, as well as the Aungier loss model, were developed for turbines that operate with conventional working fluids, such as air. Therefore, their application to non-conventional working fluids, such as CO_2 mixtures, may result in reduced prediction accuracy. The full details of the iterative solution process of the mean-line performance approach are explained in Appendix A.

2.2. CFD model

The outputs of the mean-line flow path design model are used to create the 3D blade geometry and initiate the numerical simulations. The numerical model is a 3D, multi-stage CFD model with a single flow passage for each blade row as shown in Fig. 1. Each stator–rotor interface is modelled as a mixing plane with an appropriate pitch ratio based on the number of blades, which is commonly used for steady-state simulations with a reasonable level of accuracy and reliability [25]. The flow model is based on Reynolds averaged Navier Stokes equations (RANS) while the k–ω SST turbulence model was selected to close the system of equations as it has been shown to provide reasonable predictions for turbomachinery applications [26]. The governing equations of the flow model as well as the turbulence model can be found in [27]. The boundary conditions applied to this model at the inlet are the total pressure, total temperature, normal velocity vector, and 5% turbulence intensity. At the outlet, the static pressure was applied while the mass-flow rate is calculated and then verified against the mean-line model. The steady-state assumption is commonly used for turbomachinery applications, especially when the flow is subsonic, where it is not expected to have shockwaves crossing the rotor and stator flow domain boundaries, and the differences between steady-state and unsteady performance results are negligible [28,29].

The CFD simulations were performed using ANSYS CFX 2020R2, employing a finite volume discretisation approach and a high-resolution advection scheme. The computational time for each case of the 14-stage model, with the recommended mesh size at off-design operating conditions, is approximately 19 h. This was achieved using a single computing node within a high-performance computer featuring a 48-core processor of 3.00 GHz base frequency and 384 GB of RAM.

The 3D blades were generated based on the mean-line design results as discussed in the author's previous publication [30]. The blades are straight without twist or taper angles due to the small blade aspect ratio. During the turbine design phase, the 3D blade design is iteratively adjusted to ensure the design delivered the required mass-flow rate at the design pressure ratio. The resulting 3D blade geometry is also evaluated using a structural finite element analysis simulation to ensure that mechanical stresses are within acceptable limits, with the fillet at the base of the blade adjusted to meet the stress constraints. Further enhancements to the 3D blade geometry are achieved through blade shape optimisation, which aims to ensure the turbine matches the intended cycle operating conditions while maximising aerodynamic performance [31]. The thermodynamic properties of the working fluid are introduced into the CFD model using look-up tables that cover the expected pressure and temperature ranges. The selected pressure range is between 10 and 300 bar to cover local variations within the solution domain. Similarly, the temperature range is set between 400 and 1000 K. Different sizes of the lookup tables have been examined ranging between 100×100 and 500×500 points while the variations in the model results were found to be negligibly small above 200×200.

To evaluate the performance at the off-design conditions, the same numerical setup was used, and either the inlet or outlet pressures are varied to change the pressure ratio across the turbine. Because of the possibility for increased turbulence and flow separation at off-design operating conditions as a result of increased incidence angles, a grid independence study was carried out at the design point and this is re-assessed to ensure mesh independence for the off-design simulations.

The mesh is structured and generated using ANSYS TurboGrid to provide a suitable mesh topology for the proposed turbine application that allows achieving the mesh convergence with minimal computational effort. The relation between the number of grid points obtained using different grid structures and the total-to-total efficiency is shown in Fig. 2 for the design point and for an operating point that corresponds to 88.5% of the design flow coefficient. At the design point, the convergence of the total-to-total efficiency can be achieved at 600,000 nodes per stage with a tolerance as low as 0.05% relative to the finest mesh. However, the off-design operating condition requires a finer mesh structure to accurately represent the case. For this study, a tolerance less than 0.2% is assumed to be sufficient and at this point the selected mesh structure requires 2.8 million grid points per stage, which is almost four times higher than the design point. Using the mesh size used for the design point calculation could introduce error in the total-to-total efficiency by up to 0.5%. Although, this tolerance could be accepted for some studies as it is not significantly large when compared to the efficiency drop at off-design conditions. For example, the drop in efficiency could be up to 15% of the design total-to-total efficiency for a 11.5% reduction in the flow coefficient compared to the design point.

A more detailed mesh study is also conducted to investigate the effect of y^+ on the predictions obtained from the model, specifically at the part-load operation where significant flow recirculation is expected. In this regard, four different grid structures are defined based on different y^+ values, element growth rates, and the number of grid points

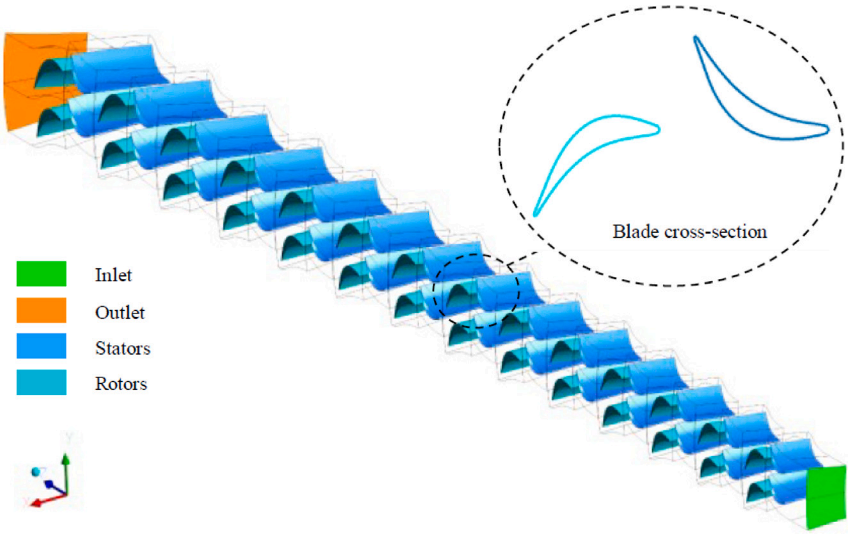

Fig. 1. CFD domain of the 14-stage turbine design along with a cross-section of the 7th stage.

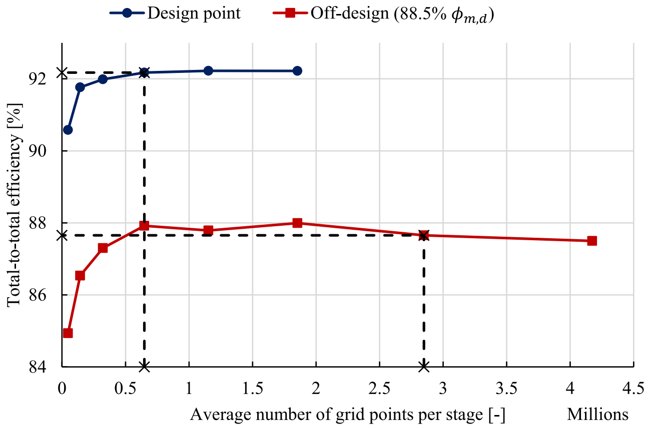

Fig. 2. Results of mesh sensitivity at design and off-design operating points for a 5-stages 130 MW design operating with CO_2/SO_2 mixture.

in the span-wise direction, as summarised in Table 2. The calculated number of grid points for the selected grids range between 0.2 to 3.25 million. The selected grid structures are applied to a 4-stage turbine designed with the boundary conditions shown in Table 4. The results are compared by considering the blade loading diagrams at the mid-span of each stage in order to assess where flow separation is predicted by each mesh at part-load, as shown in Fig. 3. It can be seen from the figure that the results of the four meshes are coincident for the first two stages, while some discrepancies are observed in the downstream stages which stems from the increased incidence in these stages. For the 3rd and 4th stages, the results obtained using Grid 3 and Grid 4 are in good agreement, although Grid 1 and Grid 2 exhibit some differences. Overall, the results indicate that Grid 3 can be selected for the part-load simulations with a good level of confidence in the results. It is noted that utilising y^{+} values lower than 1 may not be essential for simulating off-design performance, since wall functions can achieve a comparable level of accuracy to Grid 4 where $y^{+} < 1$.

3. Methodology verification

The mean-line and CFD performance prediction models have been verified against a 4-stage 700 kW axial air turbine [32] where experimental results were available in the literature at off-design operating conditions. The flow path design is initially mapped at the design point using the in-house mean-line design tool presented in the authors previous publication [33]. The boundary conditions are summarised in Table 3. Subsequently, the aerodynamic performance is evaluated at different operating conditions using both the mean-line and CFD models to generate the performance maps for the selected design.

The performance maps, obtained using both mean-line (ML) and CFD models, are compared to the numerical and experimental published results as shown in Fig. 4, where the numerical results are obtained using a through-flow turbine model. The relation between the reduced mass flow rate, and the total-to-total pressure ratio (PR_{tt}) (i.e., the ideal gas form of the flow and head coefficients) is presented in Fig. 4(a), while the total-to-static stage efficiency (η_{ts}) is presented against the total-to-total pressure ratio in Fig. 4(b). The pressure ratio and reduced mass flow rate characteristic line show good agreement between the mean-line model and both numerical and experimental data, with deviations of around 2.2% and 3.3% at a pressure ratio of around 1.6. The CFD results show a similar trend compared to both experimental and numerical results however, the reduced mass flow rate is slightly shifted upward possibly due to the differences resulting from mapping out the original turbine design to conduct the off-design analysis. The obtained deviations between the CFD and both experimental and numerical results are in the range of 5.3% and 6.4% at a pressure ratio of 1.6.

By comparing the mean-line performance results to the published results presented in Fig. 4(b), larger discrepancies are observed in the efficiency values, particularly at part-load operating conditions. At a pressure ratio of 1.6, deviations between the mean-line model and both experimental and numerical total-to-static efficiency reach up to 6%. These deviations increase further, reaching their maximum at a pressure ratio of 1.2, with deviations of 39% and 29% compared to experimental and numerical results, respectively. The increase in deviation is likely due to separation effects and losses not accounted for in the mean-line design model, such as windage losses. Flow reversal and flow separation have been reported in both the experimental and numerical results, as indicated in a referenced study [32]. The CFD model shows better coincidence with both experimental and numerical results in terms of total-to-static efficiency. The deviation in efficiency at the design point is within 1.7% and 2.9% compared to the experimental and numerical results, respectively. Similar deviations are observed between the CFD results and analytical data across the tested range of operating conditions, although the experimental results show a sharper efficiency drop at pressure ratios below 1.4. At a pressure ratio of 1.3, there is an efficiency difference of 4% and 3% compared

Table 2
Details of the selected grid structures to evaluate the mesh sensitivity at off-design.

Grid	Average y^+	Growth rate	Number of used grid points in the spanwise direction	Total number of used grid points per row (million)
Grid 1	200	1.3	22	0.20
Grid 2	100	1.2	33	0.62
Grid 3	30	1.2	44	1.81
Grid 4	0.75	1.1	77	3.25

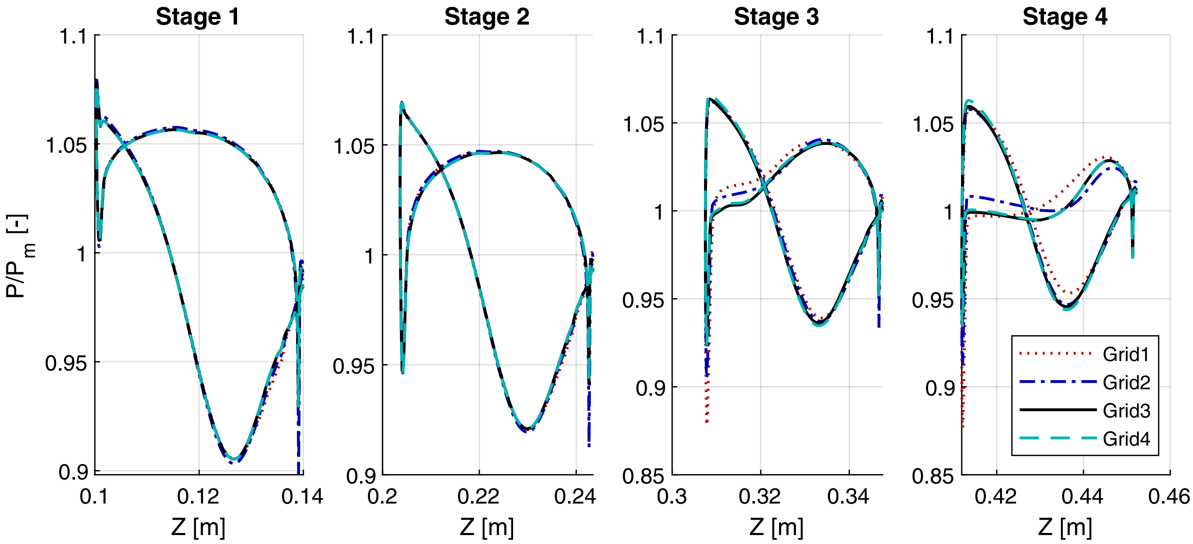

Fig. 3. Mesh sensitivity of the rotor blade pressure distribution at mid span to four different grid structures in a 4-stage $s\text{CO}_2-\text{SO}_2$ model operating at 88.5% of the design flow coefficient.

Table 3
Boundary conditions for the air verification case [32].

Parameter	Description	Unit	Value [32]
T_{01}	Stator total inlet temperature	[K]	413
P_{01}	Stator total inlet Pressure	[MPa]	0.26
PR	Pressure ratio	[–]	2.54
n	Number of stages	[–]	4
$\dot{m}$	Mass flow rate	[kg/s]	7.8
t_{cl}	Clearance gap	[mm]	0.24
N	Rotational speed	[kRPM]	7.5
$\dot{W}$	Power output	[MW]	0.7

to the experimental and numerical results, respectively. At a pressure ratio of 1.2, a difference of 11% and 1% is observed.

Compared to the mean-line model, the CFD model predicts a sharper drop in reduced mass flow rate at low-pressure ratios. It has been found that the mean-line model overpredicts the performance at very low reduced mass flow rates compared to all models. The deviation between the mean-line and CFD at a pressure ratio of 1.3 in the total-to-static efficiency is 24.4 percentage points.

4. Results and discussions

This section presents the assessment of the aerodynamic performance of the CO_2/SO_2 flow path under off-design conditions, utilising both the mean-line performance model and CFD simulations. It also aims to evaluate the suitability of the mean-line loss model by comparing the predictions to the CFD simulation results. To achieve these objectives, the turbine is simulated across a wide range of operating conditions and the performance predictions are compared. The 3D flow characteristics obtained from the CFD simulations are analysed in an attempt to investigate potential features that may lead to the observed discrepancies between the two models. This includes comparing the off-design performance predictions for multiple turbine flow path designs.

Table 4
Operating conditions of the 130 MW axial turbine operating with the CO_2/SO_2 mixture.

Parameter	Unit	value	Parameter	Unite	value
Inlet Temperature [T_{01}]	°C	700	Inlet Pressure [P_{01}]	MPa	23.9
Outlet pressure [P_{03}]	MPa	8.15	Mass flow rate [$\dot{m}$]	kg/s	827.06

Furthermore, the validity of similitude theory is examined for various CO_2 mixtures and molar fractions and comparing these to predictions obtained from the scaling laws.

4.1. Performance maps of the CO_2/SO_2 turbine

The off-design performance is evaluated for an axial turbine operating with the $80\%\text{CO}_2/20\%\text{SO}_2$ mixture. Details of the turbine design are presented in the authors' previous work where the flow path was designed to operate within a pre-compression cycle for a 100 MW_e CSP plant [34]. The mixture was selected for the SCARABEUS project, from three candidate mixtures, based on cycle optimisation results alongside consideration of thermal stability and environmental factors. A summary of the turbine boundary conditions is provided in Table 4. The flow path design was obtained using an in-house mean-line design tool assuming a zero incidence angle with an inlet flow angle $\alpha_1 = 0$, while the flow coefficient, load coefficient and degree of reaction were set to 0.5, 1 and 0.5 respectively. The optimum aerodynamic performance was obtained when fourteen stages are selected for the design. In this case, the hub diameter is 624 mm and the flow path shaft length is approximately 1.8 m. A summary of the key geometrical parameters of the first and last turbine stage is provided in Table 5.

The turbine performance maps of the 14-stage $80\%\text{CO}_2/20\%\text{SO}_2$ are presented in Fig. 16 for different blade Mach numbers (Ma_b) of 0.41, 0.43 and 0.46. The relation between the flow coefficient ϕ_m and the head coefficient is presented in Fig. 5(a) while the relation between the flow coefficient and the total-to-total efficiency is presented in Fig. 5(b).

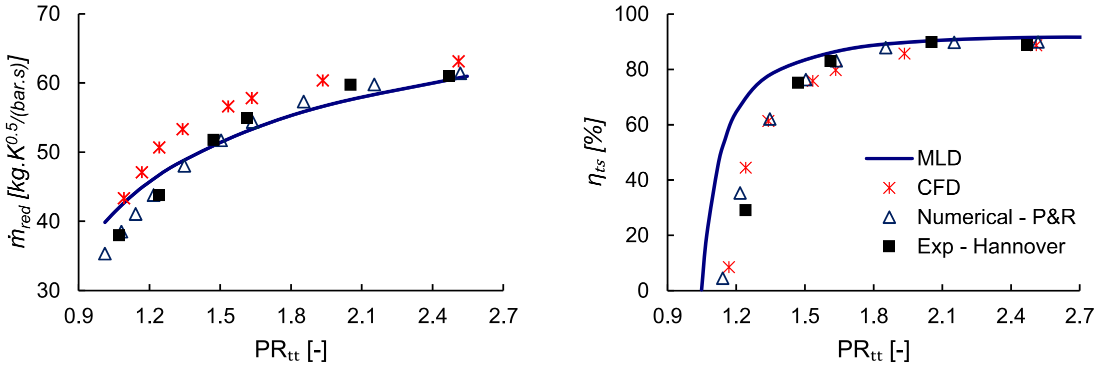

(**a**) (**b**)

Fig. 4. Verification results of the off-design performance mean-line and CFD model against 700 kW air turbine (a) reduced mass flow rate ($\dot{m}_{red}$) versus the total-to-total pressure ratio (PR_{tt}) (b) total-to-static efficiency (η_{ts}) versus total-to-total pressure ratio (PR_{tt}) [32].

Table 5
Flow path design details for 14-stage turbine design operating with the CO_2/SO_2 mixture.

Parameter	14-stage		Parameter	14-stage	
	1st stage	last stage		1st stage	last stage
Number of stages [–]	14		(R) Inlet tip diameter [mm]	735	853
(S) Number of blades	53	42	(R) Outlet tip diameter [mm]	738	860
(R) Number of blades	58	47	(S) Inlet blade height [mm]	54	113
Radial tip clearance [mm]	0.52	0.60	(S) Outlet blade height [mm]	55	114
(S) Inlet blade angle [°]	0	−4.6	(R) Inlet blade height [mm]	56	115
(R) Relative inlet blade angle [°]	0	−15.5	(R) Outlet blade height [mm]	57	118
(R) Relative outlet blade angle [°]	64.90	65.92	(S) Inlet area [m^2]	0.12	0.26
(R) Average chord length [mm]	48	66	(R) inlet area [m^2]	0.12	0.27
S) Average chord length [mm]	43	59	(R) Outlet area [m^2]	0.12	0.28
Hub diameter [mm]	624		(R) Inlet blade speed [m/s]	107	117
(R) Inlet mean diameter [mm]	682	747	(R) Outlet blade speed [m/s]	107	118
(R) Outlet mean diameter [mm]	683	751	(R) Aspect ratio [–]	1.2	1.8
Total-to-total efficiency [%]	93.86				

It is important to note that this design is intended for a synchronous machine that operates at a fixed rotational speed of 3000 RPM. The different blade Mach numbers are obtained by keeping the rotational speed constant while varying the inlet turbine temperature by a 100 °C interval.

By comparing the results obtained from the mean-line and CFD, it becomes evident that there is a difference in the predicted head coefficient between the two models. At a blade Mach number of 0.41, the difference between the mean-line and CFD results is found to be 1.5% and 5% at 90% and 102% of the design flow coefficient, respectively. This corresponds to a flow coefficient range of 0.030 to 0.034. However, this difference increases at higher blade Mach numbers, with a difference of 9% and 7% observed at 90% and 102% of the design flow coefficient respectively. This observation shows that the deviation between the mean-line and CFD models increases as we go further from the design point.

Significant discrepancies are observed in the predicted total-to-total efficiency between the mean-line model and CFD simulations (Fig. 5(b)). The performance results obtained by the mean-line model and CFD simulations agree when operating at mass flow rates close to the design point. However, deviations tend to increase significantly as the mass flow rate deviates from the design point.

The total-to-total efficiency remains relatively constant between 99% and 102% of the design flow coefficient, but it decreases significantly at lower mass flow rates. Varying the mass flow rate between 99% and 102% of the design flow coefficient, which corresponds to a flow coefficient range of 0.033 to 0.034, results in a maximum deviation of 1% between the efficiency predicted by the mean-line model and the CFD results. However, reducing the mass flow rate further from 99% to 90%, within a flow coefficient range of 0.030 to 0.033, results in deviations between the ML and CFD models ranging from a minimum of 8% to a maximum of 14% for blade Mach numbers of 0.41 and 0.46, respectively. Moreover, as the operating mass flow rate is further reduced, differences in the efficiency of up to 26% are observed at a blade Mach number of 0.41 and a flow coefficient of 0.026.

Based on the CFD results, this turbine can operate down to 90% of the design flow coefficient with a total-to-total efficiency in excess of 80% at a blade Mach number of 0.41. On the other hand, according to the ML predictions, the turbine can operate down to 90% of the flow coefficient with a total-to-total efficiency of over 90%. These deviations in the total-to-total efficiency indicate that some of the flow features and losses are not well captured by the mean-line model, resulting in an over-prediction of the total-to-total efficiency compared to the CFD results, particularly at low mass flow rates. In an attempt to understand the source of these discrepancies, the differences between the mean-line and CFD models are further investigated in the following sub-sections.

4.2. Comparative analysis of the mean-line and CFD models

In this subsection, a detailed analysis has been conducted for each stage of the proposed turbine model, examining the key performance parameters such as the total-to-total efficiency and the total enthalpy loss coefficient using both models. The total enthalpy loss coefficient is defined as the summation of the stator and rotor loss coefficient for each turbine stage ($\zeta_S + \zeta_R$). The results presented in this section are obtained by analysing the turbine at a fixed outlet pressure while varying both the inlet pressure and mass flow rates for both the ML and CFD results. The flow coefficients are set at 90%, 98%, 100%, and 102% of the design flow coefficient, as shown in Fig. 6.

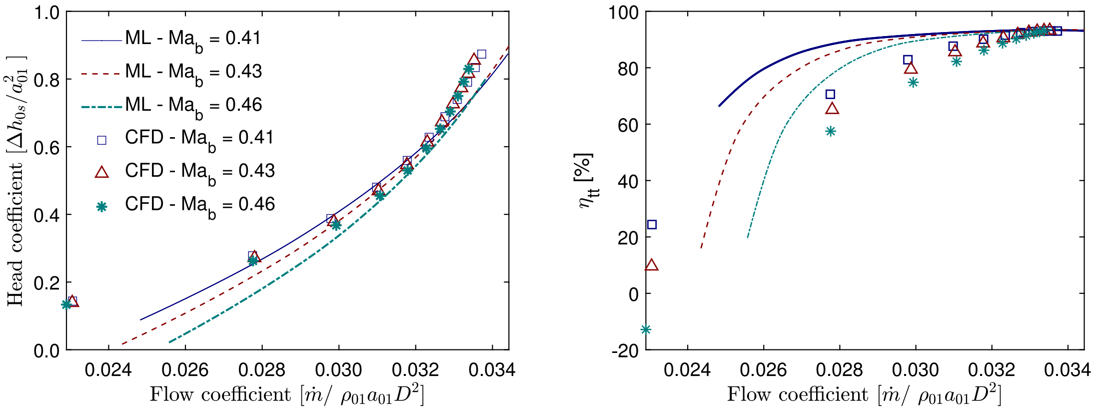

(a)	(b)

Fig. 5. Performance maps of the 14-stage CO_2/SO_2 flow path using CFD and ML models; flow coefficient versus (a) head coefficient (b) total-to-total efficiency.

At 90% of the design flow coefficient, slight differences are observed in the predicted loss coefficients and stage efficiency for both the ML and CFD models for the first seven stages. However, further downstream significant deviations between the mean-line and CFD results are observed across the later stages; where the maximum deviation is observed at the last turbine stage as illustrated in Fig. 6(a). The difference in the stage efficiency between the ML and CFD models reaches a maximum of 4% across the first seven stages. Moving further downstream, the percentage difference increases from 4 to 37% at the 7th and 14th stage, respectively. This corresponds to a total-to-total efficiency of 80% (predicted by the ML model) compared to 43% (predicted by the CFD model). The 37% difference in total-to-total efficiency is attributed to a deviation of 80% in the predicted loss coefficients compared to the CFD results.

Increasing the flow coefficient from 90% to 98% of the design point and beyond leads to a better agreement between the ML and CFD models across a larger number of stages. However, deviations between the two models are observed after the 13th stage as shown in Fig. 6(b). Operating at 98% of the design flow coefficient results in a maximum efficiency difference of 2.6% over the first thirteen stages. The efficiency difference gradually increases, reaching 6.8% at the last turbine stage (the 14th); this corresponds to a 51% increase in the total loss coefficient. Operating at mass flow rates higher than the design point, up to 130% of design flow coefficient, results in a maximum difference of 2.3% between the ML and CFD results, as depicted in Fig. 6(c) & 6(d).

In view of the fact that off-design operation typically results in non-zero incidence (the mismatch between the inlet flow angle [α_1] and the blade leading edge [α_1]) and deviation angles (the difference between the outlet flow angle and the blade angle [$\delta = \beta_3$-β_3']), it is important to quantify these angles with respect to both ML and CFD models. Fig. 7(a)–7(b) present the incidence angles estimated by the ML and CFD models at 90% and 102% of the design flow coefficient; which are equivalent to 434 and 1053 kg/s respectively. In the CFD model, the area average velocity components are calculated at the interface between the blade rows. These components are used to calculate the absolute and relative flow angles which are compared to the blade design angles to calculate the incidence and deviation angles.

These two cases are selected to represent the extreme operating conditions. Operating at a mass flow rate that is lower than the design value results in negative incidence angles. According to the ML model, the incidence angle increases from −17° to −53° in the stator blade row and from −16 to −43° in the rotor blade row as the flow moves through the turbine. Both the CFD and ML models result in similar incidence angles across the stages, with a maximum difference for the stator row of 5.4° of the 7th and a maximum for the rotor row of 2.5° at the 1st stage. On the other hand, operating at 102% of the design flow coefficient leads to positive incidence angles due to the increased axial velocity compared to the design point. The ML and CFD models show a maximum difference of 5.2° in the incidence angle for the last turbine stage.

Similarly, the deviation angle is obtained by both models at 90% and 102% of the design flow coefficient. At 102% of the design flow coefficient, a maximum deviation angle (δ) of −1.4° is observed. At 90% of the design flow coefficient, the maximum difference in the predicted deviation angle between the ML and CFD models is found to be 1.86° in rotor of the last turbine stage. This proves that the deviation angle does not change significantly with the operating conditions, and hence, it is not a critical parameter in this analysis compared to the incidence angle.

The velocity triangles obtained from the ML and CFD models are compared as shown in Fig. 8 at 90%, 100% and 102% of the design flow coefficient for the 1st, 7th and 14th stages. At the design point, there is a consistent observation of similar velocity triangles across all stages, resulting in uniform power production from each stage (Fig. 8). However, as the flow coefficient reaches 90% of the design value, the axial velocities of the flow decrease from the 1st to the 14th stages, leading to a decrease in whirl velocity resultant and power generation between the turbine stages. As the mass flow rate increases along the turbine blades, the downstream axial velocity component also increases, resulting in a greater whirl velocity resultant and, ultimately, an increase in power generation across the stages. It is worth concluding here that both the ML and CFD models demonstrate remarkably similar velocity triangles at the off-design conditions of operating with 90% and 102% of the design flow coefficient.

It is evident from the previous results that the ML and CFD models demonstrate similar predictions for flow angles and velocity triangles. However, there are significant deviations in efficiency between the ML model and CFD results at lower mass flow rates, while showing a good agreement at higher mass flow rates. Despite predicting similar flow angles, even small deviations in flow angles can have a substantial impact on the predicted efficiency by the ML and CFD models. At lower mass flow rates, increased deviations in flow angles result in higher profile losses, making the flow more prone to separations; where flow separations are three-dimensional phenomena that are captured through CFD simulations but are not predicted in the mean-line loss model.

4.3. Three dimensional flow characteristics

The 3D flow features are presented in this section to further investigate the discrepancies between the mean-line and CFD results, specifically at low mass flow rates. The flow structure at 90.1% of the design flow coefficient is investigated by considering the Mach number

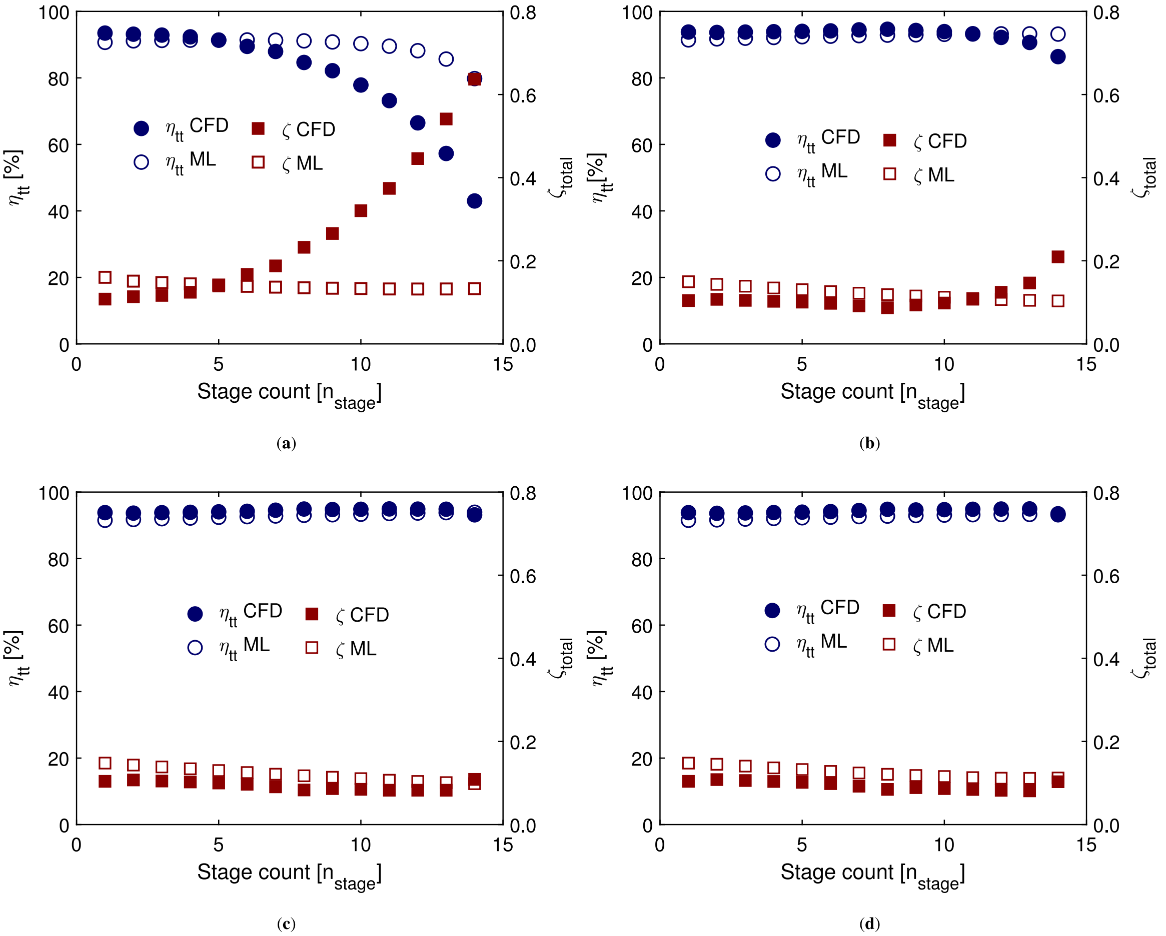

(a)

(b)

(c)

(d)

Fig. 6. The total-to-total turbine efficiency [η_{tt}] and loss coefficient [ζ_{total}] change versus the different turbine stages [n_{stage}] at (a) 90% (b) 98% (c) 100% (c) 102% of the design flow coefficient, evaluated at the blade mid-span.

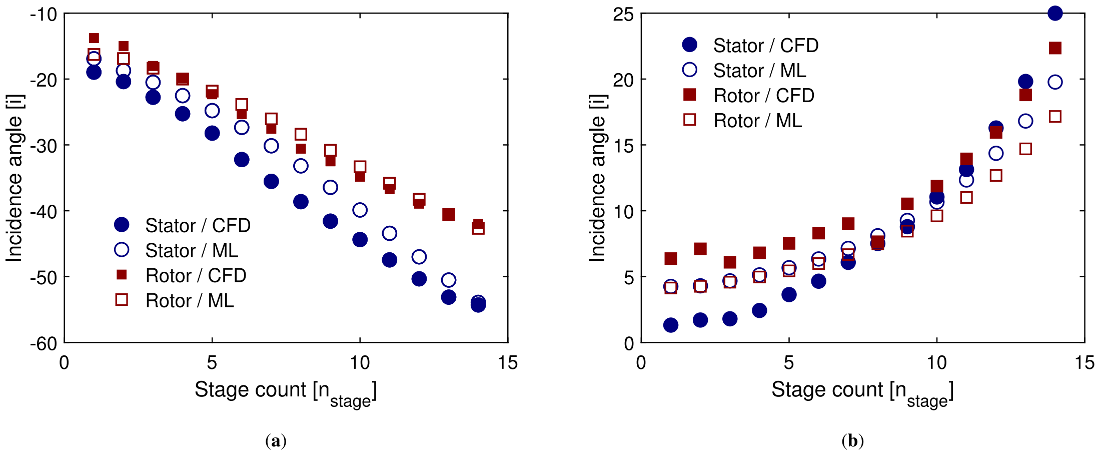

(a)

(b)

Fig. 7. Incidence angle (i) versus the stage count [n_{stage}] at (a) 90% (b) 102% of the design flow coefficient, evaluated at the blade mid-span.

distribution as shown in Fig. 9. Two passages are presented at three different spanwise locations, specifically at 5% offset from the hub surface, at mid-span, and at 5% offset from the tip surface, defined as a percentage of the span length. The simulation is completed for all of 14 stages; however, in the figure certain stages are removed to enhance clarity and emphasise the significant characteristics observed in the first, middle, and last stages. This selective cropping allows for better visualisation and to focus on the key features of interest.

It can be seen from the figure that no flow separation is observed in the first stages due to the good match between the flow and blade angles. As indicated in the figure, downstream stages experience flow separation at part-load, starting from the 6th stage at mid-span and near the hub surface. The separation regions grow along the streamwise direction due to increasing the incidence angle as reported in Fig. 7 and observed in Fig. 9 for the last two stages. Near the blade tip, the flow recirculation is more obvious because of the leakage flow

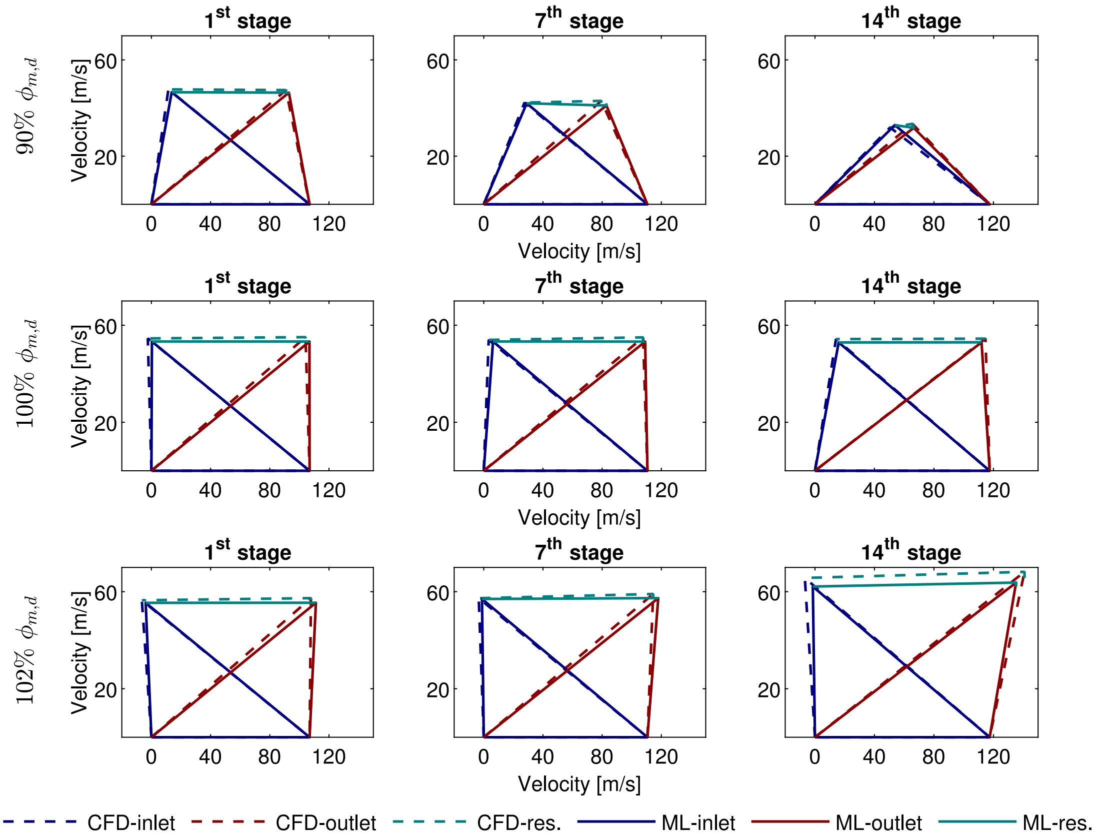

Fig. 8. Comparison between the velocity triangles of the CO_2/SO_2 flow path at 90%, 100% and 102% of the design flow coefficient, evaluated at the blade mid-span.

through the tip clearance gap. Considering the other off-design cases, it is found that the location where separation first occurs moves upstream as the mass flow rate decreases, which results in a larger number of stages being influenced by flow separation. Conversely, within the investigated operating points corresponding to a mass-flow rate that exceeds the design value, no flow separation is observed.

In order to quantify the flow separation, the volumes of negative axial velocity are evaluated for the different operating conditions and the results are shown in Fig. 10(a). In this figure, the separation volume ratio to the total flow volume is plotted against the stage number and the flow coefficient ratio. To outline the flow separation region on the map, a contour line corresponding to a volume ratio of approximately 0.1% is shown. The assumption here is that the separation effect is directly related to an increased volume ratio. By investigating the part-load operating conditions, separation regions were observed in the last stage at 98% of the design flow coefficient and propagated back to the preceding stages as the flow coefficient is further reduced. This explains the drop in efficiency, and in the power output per stage, as the mass-flow rate is reduced. At higher mass flow rates, no flow separation is observed within the fluid domain, which helps ensure minimal losses and improved aerodynamic characteristics.

A comparison is conducted between the mean-line model and CFD results where the deviations in stator and rotor enthalpy loss coefficients are reported in a similar plot, as shown in Figs. 10(b) and 10(c), respectively. By comparing the deviations in loss coefficients to the separation map in Fig. 10(a), it is evident that operating conditions where flow separation occurs are concurrent with increased deviation in the stator and rotor loss coefficients; this indicates that the presence of flow separation leads to inaccurate mean-line predictions. By comparing the deviations of the stator and rotor losses, it is found that higher deviations are observed for the stator loss coefficients, which increase as the mass flow rate decreases and the stage number increases.

The presence and effect of flow separation can be effectively captured by assessing the blade loading curves. These curves depict the pressure distribution over the blade surface at mid-span, providing valuable insights into the work produced per stage. The pressure distribution on the 1^{st}, 76th and 14^{th} rotor blades is plotted in Fig. 11 for four different operating conditions. The selected cases correspond to the design point, one higher mass flow rate (101.4% $\phi_{m,d}$), and two lower mass flow rates (90.1% $\phi_{m,d}$ and 96.1% $\phi_{m,d}$). In certain cases, such as at a flow coefficient ratio of 90.1% $\phi_{m,d}$, a crossing point can be observed. This refers to a situation where the pressure on the pressure side surface of the blade becomes lower than the pressure on the suction side surface along part of the blade's axial chord. This crossing point leads to a negative power output, significantly deteriorating the performance of the turbine stage.

It can be seen from the figure that the blade loading curve of the high mass flow coefficient case shows a positive work output across all the stages. Negative regions appear at lower mass flow coefficients, which first appear in the last stage and then propagates to the upstream stages. It is observed that the number of stages that experience negative pressure regions increases as the mass flow rate decreases due to the increased flow separation. By examining the last stage of the two low mass flow cases, it becomes apparent that the negative area becomes nearly equal to or exceed the positive area. This suggests that the blade absorbs power instead of producing power. The significant size of the negative region indicates a substantial loss in performance and raises concerns about the efficiency and functionality of the turbine stage in such operating conditions.

At higher mass flow rates the magnitude of the incidence angle increases, especially for downstream stages. However, the efficiency drop is negligible because no separation is observed over the tested range of mass flow rates. Moreover, the incidence angle for the higher mass flow rate cases is positive which means that the flow is inclined towards the pressure side of the blade which increases the blade loading and results in a larger power per stage. At part-load operation, the incidence angles approach higher magnitudes compared to the over-load operating conditions, as reported in Fig. 7. The direction of the

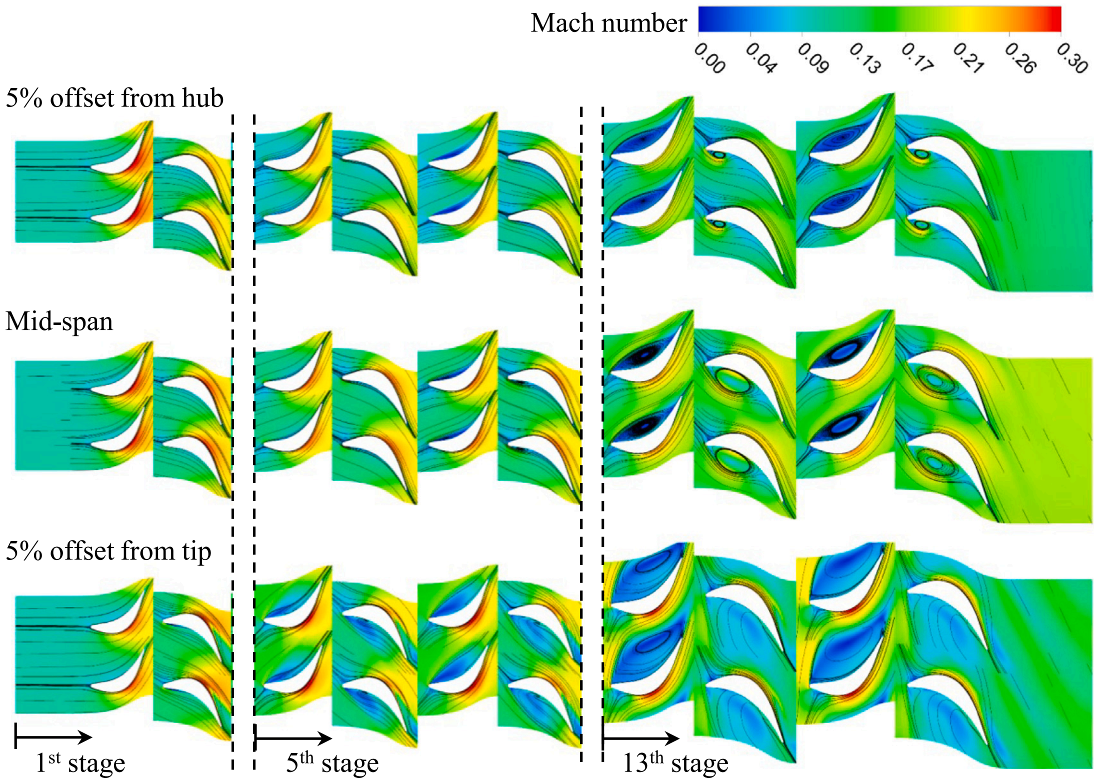

Fig. 9. Flow field obtained at off-design operating condition of 90% of the design flow coefficient near the hub, mid-plane, and near shroud surfaces.

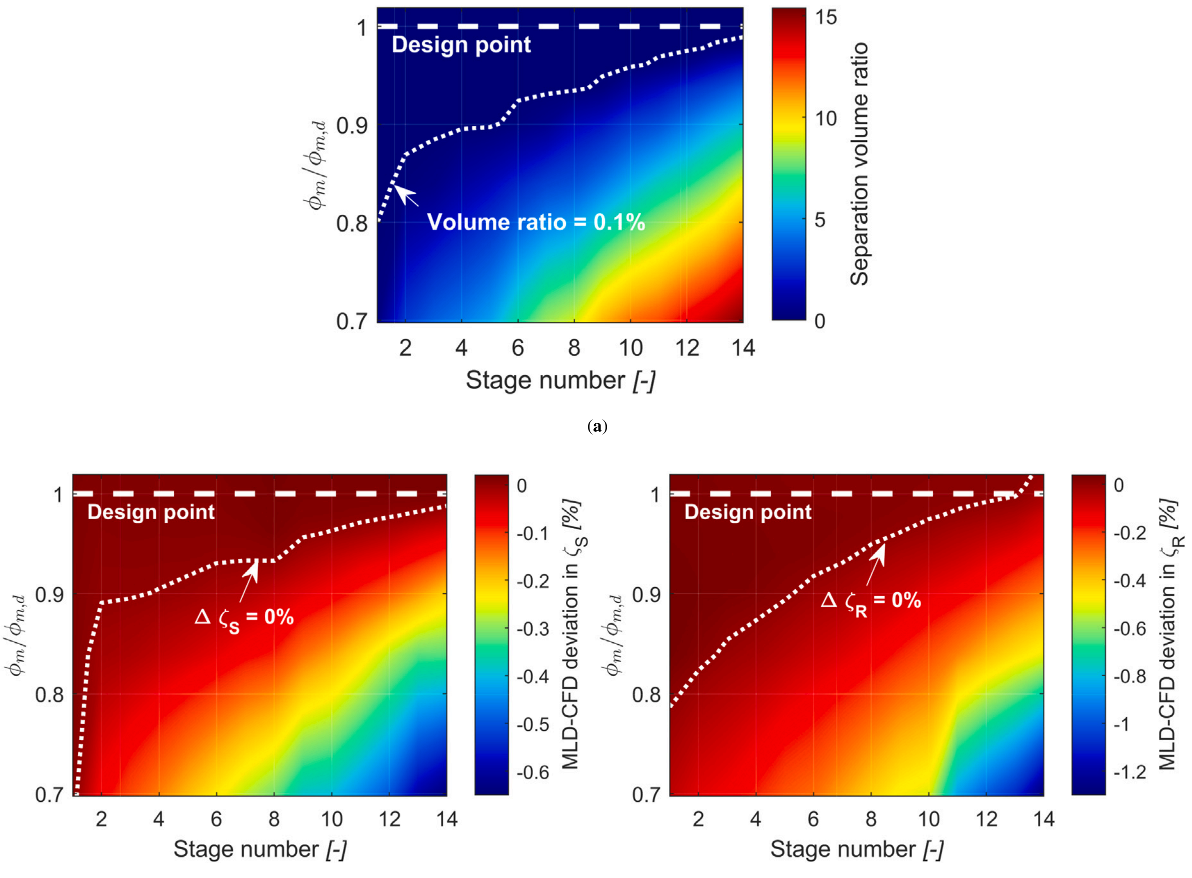

(a)

(b)

(c)

Fig. 10. Separation volume ratio (a) and the deviation between mean-line design and CFD results in terms of stator loss coefficient (b) and rotor loss coefficient (c).

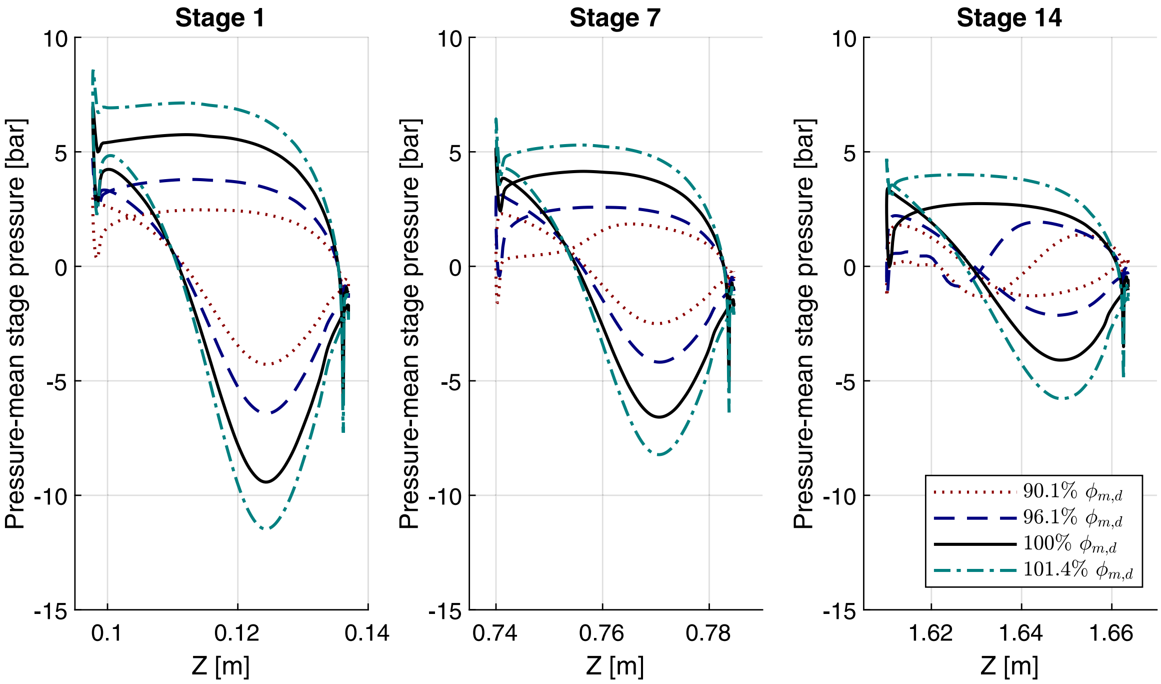

Fig. 11. Blade loading at different off-design operating conditions for the 1st, 7th, and 14th stages.

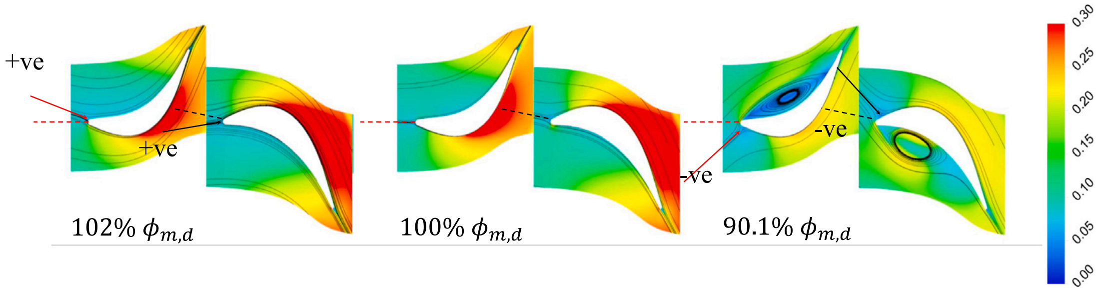

Fig. 12. Flow angle deviation illustrated by the streamlines for the higher, reference, and lower mass flow rate operating conditions.

incidence angles in these cases is negative which increases the pressure on the suction side and decreases the pressure on the pressure side of the blade resulting in flow separation at a specific incidence angle. The direction of the incidence angle is illustrated in Fig. 12 for two off-design cases: one characterised by a higher mass flow rate and another by a lower mass flow rate compared to the design value.

4.4. Comparison of off-design performance of multiple turbine flow paths

The fourteen-stage design was designed with the primary objective of optimising the design point efficiency. In order to investigate the impact of the number of stages on part-load performance and to further investigate possible deviations between the ML and CFD models, three turbine designs have been considered. The proposed designs include a minimum stage configuration of 4 stages, a maximum stage configuration of 14 stages, and an intermediate design of 9 stages. The minimum number of stages was chosen to maintain the blade peripheral speed below 180 m/s, as previously specified in [22]. The flow paths were designed using the mean-line design model using same dimensionless parameters as specified in Section 2.1, and for the same boundary conditions specified in Table 4. A comparison between the geometry of the three designs is given in Table 6.

Table 6
Comparison between the three flow paths designed with various number of stages.

Parameter	4-stage	9-stage	14-stage
Number of stages [–]	4	9	14
Hub diameter [mm]	1212.53	805.87	621.21
Inlet tip diameter [mm]	1246.12	876.72	730.34
Outlet tip diameter [mm]	1292.52	967.01	857.98
Avg. blade chord [mm]	47.05	44.32	52.93
Flow path length [mm]	521.94	991.89	1703.24
Inlet Mach number [–]	0.46	0.31	0.25
Inlet Reynold’s number [–]	9.15E+06	1.33E+07	1.66E+07

From a practical standpoint, the minimum part-load mass flow rate can be defined from the maximum allowable exhaust temperature. Considering the size and pressure levels of the proposed turbine design, stainless steel can be used for the exhaust section, which can withstand up to 500 °C while maintaining reasonable mechanical characteristics [35]. With a proper cooling system, the maximum temperature of the hot exhaust gas can be assumed to be around 600 °C. In this regard, the relation between the flow coefficient ratio to the design flow coefficient and the total-to-total efficiency, as well as the turbine exhaust temperature is presented in Fig. 13. In this figure, the performance curve is provided for the 4-stage and 14-stage designs and this is obtained using CFD results where the 600 °C temperature limit is highlighted. It can be seen from the figure that the 14-stage design can safely operate at part-load down to 94.5% of the design flow coefficient while achieving a total-to-total efficiency of 89.2%. The 4-stage design has a lower performance at part-load where the minimum part-load

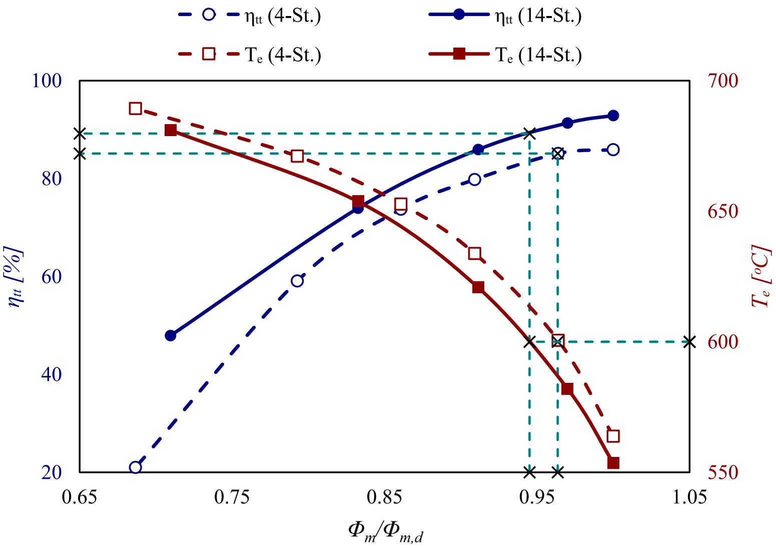

Fig. 13. The flow coefficient relative to the design flow coefficient against the total-to-total efficiency and the exhaust temperature as obtained for the 4 and 14-stage designs using CFD results.

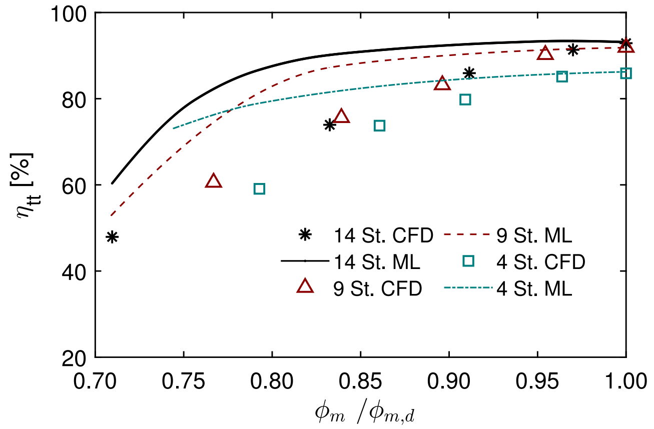

Fig. 14. The effect of changing the number of stages on the off-design performance of CO_2/SO_2 turbines based on both mean-line and CFD results.

mass flow rate is found at 96.35% of the design mass flow rate while the total-to-total efficiency at this operating point is 85.12%.

A comparison between the ML model and CFD results is performed for the three proposed designs as shown in Fig. 14. The figure demonstrates that increasing the number of stages leads to higher efficiency at both design and off-design operating conditions, assuming all other flow path design parameters remain constant. Specifically, going from 4 stages to 9 stages results in a significant improvement of 6.25% in total-to-total efficiency while increasing the number of stages from 9 to 14 stages yields a limited enhancement of 0.7% at the design point. However, the mean-line model falls short in predicting the performance at low mass flow rates for all the proposed designs. Specifically, the deviation between the mean-line design and CFD results was found to be 5.6%, 6.4%, and 8.1% for the 4, 9, and 14 stages respectively at 90% of the design flow coefficient. These deviations increase up to 18.6%, 10.9%, and 20.3% at 80% of the design flow coefficient.

4.5. Similitude analysis

In this section, an investigation of the validity of similitude scaling laws is presented across different working fluids and a range of molar fractions. To accomplish this, two additional mixtures, namely $CO_2/TiCL_4$ and CO_2/C_6F_6, were selected in addition to the CO_2/SO_2 mixture for which the turbine was originally designed. It is worth noting that these mixtures were chosen based on an earlier cycle analysis that was conducted within the SCARABEUS consortium, which demonstrated their promising potential for CSP-CO_2 cycles [3,4,36].

Furthermore, three different molar fractions are selected for each mixture: 20%, 25%, and 35% for CO_2/SO_2; 14%, 17%, and 24% for $CO_2/TiCL_4$; and 10%, 14.5%, and 20% for CO_2/C_6F_6. The selection of these molar fractions is based on the methodology presented in Salah et al. [22], where the lower bound for each dopant was specified based on a set criterion that the difference between the minimum cycle temperature and the critical temperature of the resulting mixture must be equal to or higher than 30 °C. This temperature gap is a conservative assumption made to ensure that the compression process is not carried out in close proximity to the critical point. The specific heat ratio (γ) and the compressibility factor for each mixture are summarised in a Table 7 for different molar fractions.

Three different blade Mach numbers of 0.29, 0.41, and 0.53 have been considered in this analysis. Although the turbine is a synchronous machine operating with a fixed rotational speed of 3000 RPM, a range of rotational speeds was considered for the purpose of covering a wider range of operating conditions. These blade Mach numbers correspond to rotational speeds of 2300, 3000, and 3900 RPM for the CO_2/SO_2 mixture at a 20% molar fraction. It is worth mentioning that the three different blade Mach numbers were maintained constant for the mixtures by adjusting the rotational speeds while keeping the inlet pressure and temperature unchanged. The boundary conditions used for the examined cases are given in Table 8.

The results reported in Figs. 15(a) and 15(b) show the application of similitude theory using the mean-line performance model, formulated using the real-gas form, for the three mixtures at a single molar fraction of 20%, 14% and 10% for the CO_2/SO_2, $CO_2/TiCL_4$ and CO_2/C_6F_6 respectively. It is evident that the scaling laws hold true, as all three mixtures exhibit identical trends in terms of the head coefficient and efficiency against the flow coefficient for the same blade Mach number. Moreover, the scaling laws apply across the different blade Mach numbers considered.

The validity of the scaling laws has also been investigated for various molar fractions ranging from 20% to 35% for the CO_2/SO_2 mixture, as shown in Figs. 16(a) and 16(b). The findings are consistent with the previously mentioned validity of the similitude laws for the CO_2/SO_2 mixture. The same analysis has been conducted for the $CO_2/TiCL_4$ and CO_2/C_6F_6 mixtures, yielding similar results.

Table 7
The specific heat ratio (γ) and compressibility factor [z] for the three selected mixtures.

Mixture	Molar fraction	Compressibility factor [z]	Heat capacity ratio [γ]
CO_2/SO_2	20%	0.3237	1.2163
	25%	0.3281	1.2183
	35%	0.3363	1.2226
$CO_2/TiCL_4$	14%	0.4292	1.1999
	17%	0.5247	1.1992
	24%	0.6252	1.1989
CO_2/C_6F_6	10%	0.4063	1.1537
	14.5%	0.4497	1.1390
	20%	0.4848	1.1256

Table 8
Turbine operating conditions for the three mixtures under investigation.

Boundary conditions	CO_2/SO_2	$CO_2/TiCL_4$	CO_2/C_6F_6
Turbine inlet temperature [K]	973		
Turbine inlet pressure [bar]	239		
Molar fraction [%]	20/25/35	14 /17/24	10/14.5/ 20
Rotational speed [kRPM]	3.0/2.97/2.91	2.59/2.50/2.34	2.68/2.54/2.40
Rotational speed [kRPM]	3.9/3.86/3.78	3.37/3.26/3.04	3.49/3.31/3.12
Rotational speed [kRPM]	2.12/2.09/2.06	1.83/1.78/1.65	1.90/1.80/1.70

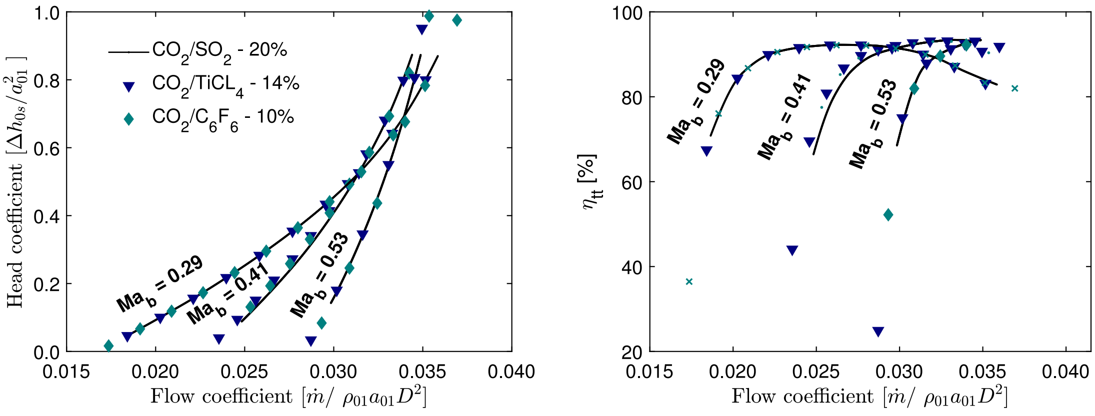

(**a**) (**b**)

Fig. 15. Performance maps of the 14-stage flow path using ML model; flow coefficient versus (a) the head coefficient (b) total-to-total efficiency operating with the CO_2/SO_2, $CO_2/TiCl_4$ and CO_2/C_6F_6 mixtures.

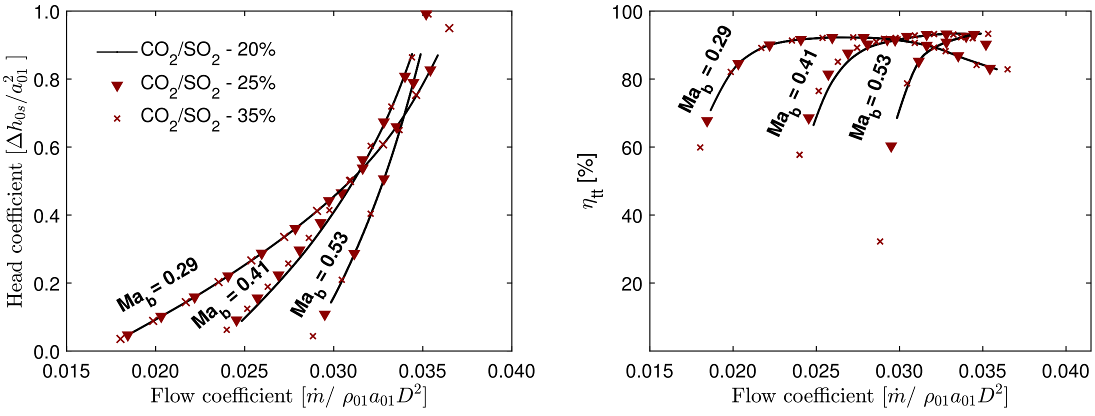

(**a**) (**b**)

Fig. 16. Performance maps of the 14-stage flow path using ML model; flow coefficient versus (a) the head coefficient, (b) total-to-total efficiency operating with the CO_2/SO_2 mixture, at 20%, 25% and 35% SO_2 by mole.

Ultimately, the validity of applying the ideal gas formulation assumption to the CO_2/SO_2 mixture has been assessed as part of this study. The detailed results of these findings are presented in Appendix B, but the main conclusions will be summarised here. It was evident that utilising the flow coefficient definition based on ideal gas assumptions introduces deviations compared to the real gas form, with a maximum deviation of 22% in the flow coefficient. Therefore, the real gas formulation should be used to obtain accurate performance maps for turbines operating with CO_2 mixtures.

5. Conclusions

The off-design performance of a large-scale 14-stage axial turbine operating with a CO_2/SO_2 mixture was investigated using mean-line analysis and CFD simulations. Both methods were validated against experimental and numerical data of a 4-stage 700 kW axial air turbine found in the literature.

Within this study, the applicability of the Aungier mean-line loss model was assessed for predicting the off-design performance of a turbine operating with a CO_2/SO_2 mixture across a range of operating conditions. This assessment involved comparing the performance predicted by the mean-line model to the results obtained from CFD simulations. Notably, at flow coefficients around 90% of the design value, deviations of 2.7% and 37% in stage total-to-total efficiency were observed between the two models for the first and last stages, respectively. The overall turbine performance showed a good agreement in terms of the head coefficient; however, significant deviations in total-to-total efficiency were observed. This can be attributed to flow separation that is not captured by the mean-line model.

Based on the results of CFD simulations, it was found that the 14-stage turbine operating with the CO_2/SO_2 mixture can achieve an efficiency of 80.2% while operating at 88.5% of the design flow coefficient during part-load operations.

Finally, the validity of similitude theory was investigated for $CO_2/TiCL_4$, CO_2/C_6F_6 and CO_2/SO_2 mixtures at multiple molar fractions. It was found that the scaling laws hold true for all examined mixtures and molar fractions across various corrected speeds. This finding may allow for the extrapolation of the analysis results to design turbines for both small and larger systems, albeit with some consideration of scaling effects that may alter the efficiency. It was found that defining non-dimensional groups based on ideal gas assumptions introduced deviations compared to the real gas form, with a maximum deviation of 22% in the calculated flow coefficient for the 14-stage turbine operating with CO_2/SO_2 mixture. This demonstrates the necessity of using scaling rules in the real gas form to generate accurate performance maps of turbines operating with CO_2 mixtures.

This work has provided the first insight into the performance predictions of the Aungier mean-line loss model at off-design conditions for large-scale axial turbines operating with CO_2 mixtures. Additionally, it provides enhanced understanding for 3D flow features in a CO_2/SO_2 130 MW scale turbine. Future work should consider supporting the results with experimental analysis to validate the obtained performance at off-design operating conditions. This would enable the calibration and tuning of the empirical constants found within the loss models to provide a more accurate representation of off-design performance and to improve the predictions for incidence losses where the existing model was found to under-predict these effects.

Declaration of competing interest

The authors declare that they have no known competing financial interests or personal relationships that could have appeared to influence the work reported in this paper.

Data availability

No data was used for the research described in the article.

Acknowledgements

This research has received funding from the European Union's Horizon 2020 research and innovation programme under grant agreement No. 814985.

Appendix A. Mean-line performance approach solution

The complete details of the mean-line performance approach are presented in this section. The solution process is iterative and starts by assuming the total inlet pressure P_{01} and flow velocity (C_1) at the inlet of the stator domain, the axial velocity at the inlet and exit of the rotor domain (C_a), and the stator and rotor enthalpy loss coefficients (ζ_S and ζ_R). The non-dimensional enthalpy loss coefficients (ζ_S and ζ_R) are defined in terms of the exit kinetic energy from each blade row as shown in Eqs. (A.1)–(A.2).

$$\zeta_S = \frac{h_2 - h_{2s}}{\frac{1}{2}{C_2}^2} \tag{A.1}$$

$$\zeta_R = \frac{h_3 - h_{3ss}}{\frac{1}{2}{W_3}^2} \tag{A.2}$$

Where C and W represent the absolute and relative flow velocities, respectively. h denotes the static enthalpy, while h_s and h_{ss} refer to the isentropic static enthalpy. The subscripts 1, 2, and 3 correspond to the conditions at the stator inlet, rotor inlet, and exit, respectively.

Using the assumed velocity (C_1) and defined inputs, the thermodynamic properties are obtained at the inlet of the stator blades. The assumed velocity is then updated based on the assumed inlet flow angle (α_1) and the steady-state energy and mass continuity equations. These equations can be expressed as:

$$h = h_0 - \frac{1}{2}C^2 \tag{A.3}$$

$$\dot{m} = \rho A C_a \tag{A.4}$$

where h_0 is the total enthalpy, A is the cross-sectional area, C_a is the axial flow velocity, ρ is the flow density.

The same procedure is applied at the rotor inlet, where absolute and relative velocities can be obtained based on the assumed axial velocity (Ca_2) and the defined blade geometry (throat-to-pitch ratio). The inlet absolute flow angle (α_2) is expressed as a function of the throat-to-pitch ratio, as shown in Eq. (A.5), and hence, the absolute and relative flow velocities are obtained as a function of the defined angles (Eq. (A.5) & (A.10)) and axial velocity (Ca_2).

$$\alpha_2 = \cos^{-1}(\mathrm{o/s})_\mathrm{S} \tag{A.5}$$

$$\beta_2 = \tan^{-1}(\tan\,\alpha_2 - \mathrm{U}_2/\mathrm{Ca}_2) \tag{A.6}$$

where $(o/s)_S$ is the throat-to-pitch ratio for the stator.

At this stage, with the utilisation of the assumed enthalpy loss coefficient (ζ_S), all thermodynamic properties are obtained and the assumed C_{a2} is updated using the continuity equation (Eq. (A.4)). Then, the assumed ζ_S can be updated based on the value calculated using the Aungier loss model [24]. Within the mean-line loss models, losses are introduced in the form of stagnation pressure loss coefficient for the stator (Y_S), which are defined as:

$$Y_S = \frac{p_{01} - p_{02}}{p_{02} - p_2} \tag{A.7}$$

where p_0 is total pressure and p is the static pressure.

Using the calculated Y_S, the assumed ζ_S is obtained by applying the relationship between the enthalpy loss coefficient and pressure coefficient that can be expressed as:

$$\zeta_S = Y_S \times \left(1 + 0.5(k\ {M_2}^2)\right) \tag{A.8}$$

where k is the specific heat ratio, and M is the Mach number.

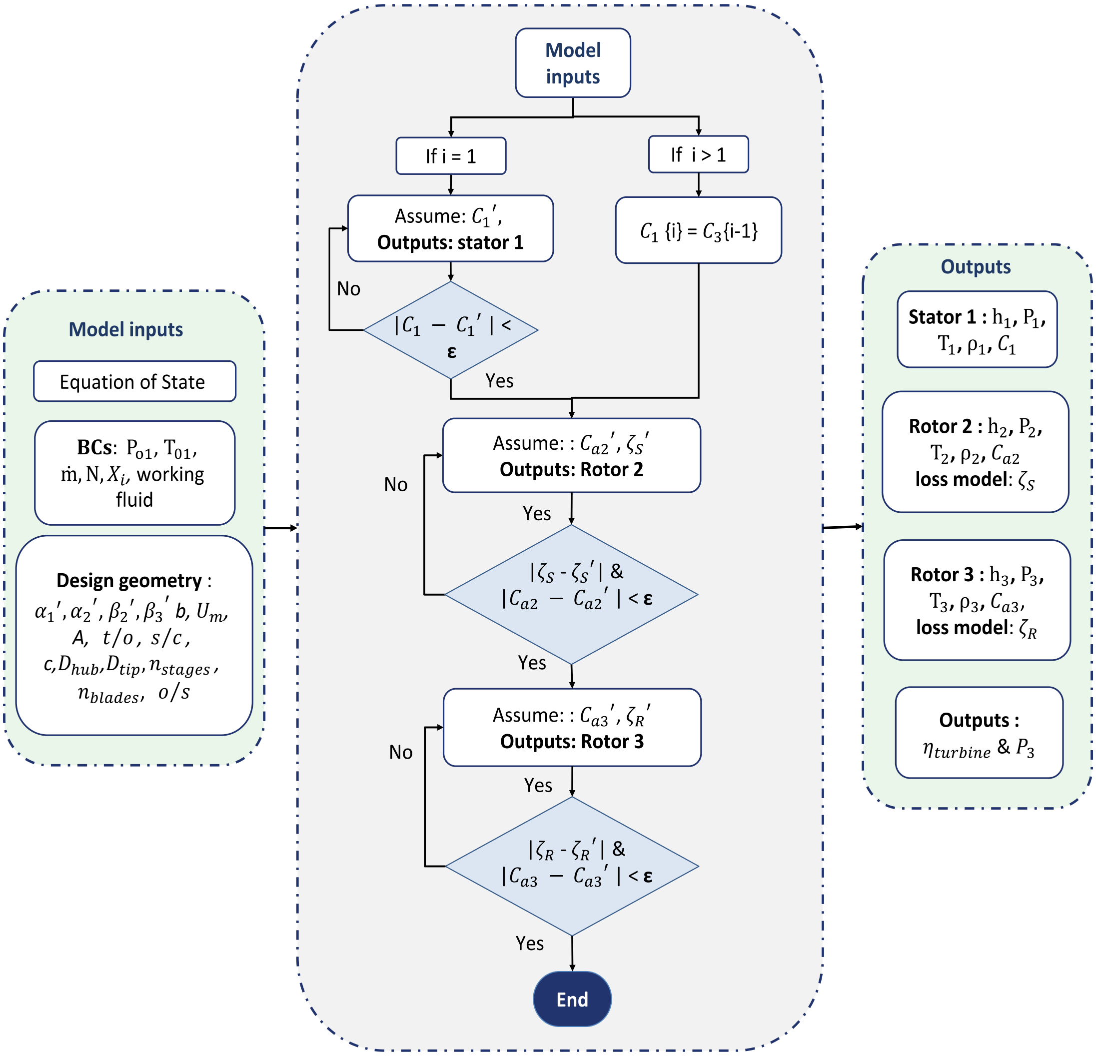

Fig. A.17. Flow chart of the mean-line off-design performance analysis methodology.

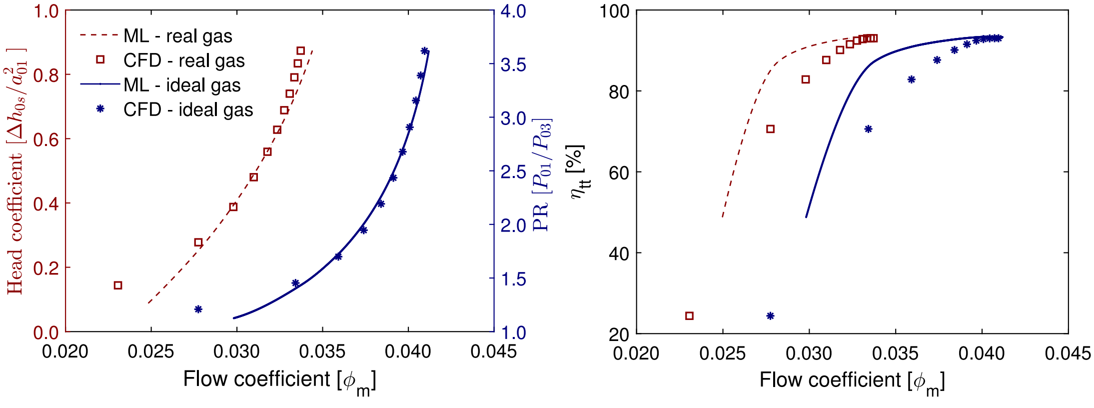

(a) (b)

Fig. B.18. Performance maps of the 14-stage CO_2/SO_2 flow path using ML and CFD models; flow coefficient defined with ideal gas and real gas forums versus (a) the head coefficient and pressure ratio (b) total-to-total efficiency.

At the last turbine station, corresponding to the rotor outlet, relative and absolute flow velocities ($C_3\&W_3$) are calculated based on the assumed axial velocity (Ca_3) and throat-to-pitch ratio ($(o/s)_R$); where the throat-to-pitch ratio is used to get the rotor exit flow angles as expressed in Eq. (A.9).

$$\beta_3 = cos^{-1}(o/s)_R \tag{A.9}$$

$$\alpha_3 = \tan^{-1}(\tan\,\beta_3 - \mathrm{U}_3/\mathrm{Ca}_3) \tag{A.10}$$

where $(o/s)_R$ is the throat-to-pitch ratio of the rotor blades.

To estimate the thermodynamic properties at the rotor outlet, the conservation of rothalpy (I), Eq. (A.11), is applied to enable the enthalpy drop across the stage to be calculated ($h_{01}-h_{03}$). At this point, all properties can be obtained, and the continuity equation (Eq. (A.4)) and the loss model correlations are used to update the assumed axial velocity (Ca_3) and enthalpy loss coefficient (Eq. (A.13)) respectively. The pressure loss coefficient Y_3 (Eq. (A.12)) is determined using the Aungier loss model and subsequently converted to the enthalpy loss coefficient using Eq. (A.13).

$$\begin{aligned} I_2 &= h_2 + 0.5W_2^2 - 0.5U_2^2 \\ I_3 &= h_3 + 0.5W_3^2 - 0.5U_3^2 \end{aligned} \tag{A.11}$$

$$Y_R = \frac{p_{02,rel} - p_{03,rel}}{p_{03,rel} - p_3} \tag{A.12}$$

$$\zeta_R = Y_R \times \left(1 + 0.5(k\ {M_3}^2)\right) \tag{A.13}$$

where $p_{0,rel}$ is the total relative pressure, U is the peripheral blade speed.

With all known properties at the rotor outlet, the static outlet pressure (P_3) is obtained. The stage total-to-total efficiency (η_{tt}) is related to the loss coefficients and thermodynamic conditions through the following definition:

$$\eta_{tt} = \left[1 + \left(\frac{\zeta_R \frac{W_3^3}{2} + \frac{C_2^2}{2}\zeta_S \frac{T_3}{T_2}}{h_{01} - h_{03}}\right)\right]^{-1} \tag{A.14}$$

where T is the static temperature and $(h_{01} - h_{03})$ is the total enthalpy drop across the stage.

This procedure is applied for the 1st turbine stage and repeated for the subsequent stages. For the subsequent stages, the inlet absolute flow velocity (C_1) is assumed to be equal to the outlet velocity of the previous turbine stage (C_3). The schematic of the mean-line off-design performance model is illustrated in detail in Fig. A.17, where the number of stages is denoted as i.

Appendix B. Supplementary results

In this section, the results of examining the validity of applying the ideal gas formulation assumption to the CO_2/SO_2 mixture and, thereby to other CO_2 mixtures, are presented. The flow coefficient is defined in this analysis using both the ideal gas form ($\dot{m}\sqrt{\gamma RT_{01}/D^2P_{01}}$) and the real gas form ($\dot{m}/\rho 01 a_{01} D^2$) to assess the accuracy of the ideal gas approximation for CO_2 mixtures. The results obtained using the real gas form are shown in Figs. B.18(a) & B.18(b). It is evident that utilising the flow coefficient definition based on ideal gas assumptions introduces deviations compared to the real gas form, with a maximum deviation of 22% in the flow coefficient. Hence, the real gas form should be used to get accurate performance maps for turbines operating with CO_2 mixtures.

References

[1] SCARABEUS project home page, 2015, Available online: http://www.scarabeusproject.eu/. (Accessed 26 November 2015).

[2] D. Bonalumi, S. Lasala, E. Macchi, CO_2-$TiCl_4$ working fluid for high-temperature heat source power cycles and solar application, Renew. Energy 147 (2020) 2842–2854, http://dx.doi.org/10.1016/j.renene.2018.10.018.

[3] G. Manzolini, M. Binotti, E. Morosini, D. Sánchez, F. Crespi, G. Di Marcoberardino, P. Iora, C. Invernizzi, Adoption of CO_2 blended with C_6F_6 as working fluid in CSP plants, in: AIP Conference Proceedings, Vol. 2445, No. 1, AIP Publishing LLC, 2022, http://dx.doi.org/10.1063/5.0086520, 090005.

[4] F. Crespi, P.R. de Arriba, D. Sánchez, A. Muñoz, Preliminary investigation on the adoption of CO_2-SO_2 working mixtures in a transcritical Recompression cycle, Appl. Therm. Eng. 211 (2022) 118384, http://dx.doi.org/10.1016/j.applthermaleng.2022.118384.

[5] G. Di Marcoberardino, E. Morosini, D. Di Bona, P. Chiesa, C. Invernizzi, P. Iora, G. Manzolini, Experimental characterisation of CO_2+ C_6F_6 mixture: Thermal stability and vapour liquid equilibrium test for its application in transcritical power cycle, Appl. Therm. Eng. 212 (2022) 118520, http://dx.doi.org/10.1016/j.applthermaleng.2022.118520.

[6] M.I. Khan, F. Asfand, S.G. Al-Ghamdi, Progress in research and technological advancements of thermal energy storage systems for concentrated solar power, J. Energy Storage 55 (2022) 105860, http://dx.doi.org/10.1016/j.est.2022.105860.

[7] E.M. Clementoni, T.L. Cox, M.A. King, Off-nominal component performance in a supercritical carbon dioxide Brayton cycle, J. Eng. Gas Turbines Power 138 (1) (2015) http://dx.doi.org/10.1115/1.4031182.

[8] M. Utamura, H. Hasuike, K. Ogawa, T. Yamamoto, T. Fukushima, T. Watanabe, T. Himeno, Demonstration of supercritical CO_2 closed regenerative Brayton cycle in a bench scale experiment, in: Proceedings of the ASME Turbo Expo, June 11–15, 2012 Copenhagen, Denmark, http://dx.doi.org/10.1115/GT2012-68697.

[9] S.A. Wright, R.F. Radel, M.E. Vernon, P.S. Pickard, G.E. Rochau, Operation and analysis of a super-critical CO_2 Brayton cycle, 2010, http://dx.doi.org/10.2172/984129.

[10] K.J. Kimball, E.M. Clementoni, Supercritical carbon dioxide brayton power cycle development overview, in: Proceedings of the ASME Turbo Expo, June 11–15, 2012, Copenhagen, Denmark, http://dx.doi.org/10.1115/GT2012-68204.

[11] J. Cho, H. Shin, H.-S. Ra, G. Lee, C. Roh, B. Lee, Y.-J. Baik, Development of the supercritical carbon dioxide power cycle experimental loop in KIER, 2016, http://dx.doi.org/10.1115/GT2016-57460.

[12] J. Moore, K. Brun, N. Evans, C. Kalra, Development of 1 MWe supercritical CO_2 test loop, in: Proceedings of the ASME Turbo Expo, June 15–19, 2015, Montreal, Quebec, Canada, http://dx.doi.org/10.1115/GT2015-43771.

[13] H. Moustapha, M. Zelesky, N. Balnes, D. Japikse, Chapter 3 - Preliminary and through flow design, in: Axial and Radial Turbines, 2003, pp. 65–95, Concepts NREC.

[14] A. Baheta, M. Sidahmed, S. Suleiman, A. Fentaye, G. Syed, Development and validation of a twin shaft industrialgas turbine performance model, ARPN J. Eng. Appl. Sci. 22 (1819–6608) (2016) 13365–13371.

[15] K. Touil, A. Ghenaiet, Simulation and analysis of vane-blade interaction in a two-stage high-pressure axial turbine, Energy 172 (2019) 1291–1311, http://dx.doi.org/10.1016/j.energy.2019.01.111.

[16] L. Zhang, W. Zhuge, Y. Zhang, T. Chen, Similarity theory based radial turbine performance and loss mechanism comparison between R245fa and air for heavy-duty diesel engine organic Rankine cycles, Entropy 19 (1) (2017) 25, http://dx.doi.org/10.3390/e19010025.

[17] A. Zhou, J. Song, X. Li, X. Ren, C. Gu, Aerodynamic design and numerical analysis of a radial inflow turbine for the supercritical carbon dioxide Brayton cycle, Appl. Therm. Eng. 132 (2018) 245–255, http://dx.doi.org/10.1016/j.applthermaleng.2017.12.106.

[18] N. Peng, E. Wang, F. Meng, Off-design performance comparison of single-stage axial turbines using CO_2 and zeotropic mixture for low-temperature heat source, Energy Convers. Manage. 213 (2020) 112838, http://dx.doi.org/10.1016/j.enconman.2020.112838.

[19] M. White, A.I. Sayma, The application of similitude theory for the performance prediction of radial turbines within small-scale low-temperature organic rankine cycles, J. Eng. Gas Turbines Power 137 (12) (2015) http://dx.doi.org/10.1115/1.4030836.

[20] D. Hu, S. Li, Y. Zheng, J. Wang, Y. Dai, Preliminary design and off-design performance analysis of an Organic Rankine Cycle for geothermal sources, Energy Convers. Manage. 96 (2015) 175–187, http://dx.doi.org/10.1016/j.enconman.2015.02.078.

[21] Simulis thermodynamics, in: Available online:. (Accessed 13 November 2019), 2019, http://www.prosim.net/en/software-simulis-thermodynamics-mixture-properties-and-fluid-phase-equilibria-calculations-3.php.

[22] S.I. Salah, F. Crespi, M.T. White, A. Muñoz, A. Paggini, M. Ruggiero, D. Sánchez, A.I. Sayma, Axial turbine flow path design for concentrated solar power plants operating with CO_2 blends, Appl. Therm. Eng. 230 (2023) 120612, http://dx.doi.org/10.1016/j.applthermaleng.2023.120612.

[23] O. Aqel, M.T. White, A.I. Sayma, Binary interaction uncertainty in the optimisation of a transcritical cycle: Consequences on cycle and turbine design, in: 14th European sCO$_2$ Conference for Energy Systems, 2021-Online.

[24] R.H. Aungier, Turbine Aerodynamics: Axial-Flow and Radial-Flow Turbine Design and Analysis, ASME Press, 2006, http://dx.doi.org/10.1115/1.802418.

[25] L. Mangani, E. Casartelli, L. Hanimann, M. Wild, N. Spyrou, Assessment of an implicit mixing plane approach for pump-turbine applications, IOP Conf. Ser. Earth Environ. Sci. 22 (2) (2014) 022003.

[26] P.E. Smirnov, F.R. Menter, Sensitization of the SST turbulence model to rotation and curvature by applying the Spalart–Shur correction term, J. turbomach. 131 (4) (2009) http://dx.doi.org/10.1115/1.3070573.

[27] D.C. Wilcox, et al., Turbulence Modeling for CFD, Vol. 2, DCW industries La Canada, CA, 1998.

[28] S. Yoon, T. Vandeputte, H. Mistry, J. Ong, A. Stein, Loss audit of a turbine stage, J. Turbomach. 138 (5) (2016) 051004, http://dx.doi.org/10.1115/1.4032138.

[29] A.P. Wheeler, J. Ong, A study of the three-dimensional unsteady real-gas flows within a transonic ORC turbine, in: Proceedings of the ASME Turbo Expo, June 16–20, 2014 Düsseldorf, Germany, American Society of Mechanical Engineers, http://dx.doi.org/10.1115/GT2014-25475.

[30] A.S. Abdeldayem, S.I. Salah, O. Aqel, M.T. White, A.I. Sayma, Design of a 130 MW axial turbine operating with a supercritical carbon dioxide mixture for the SCARABEUS project, in: 15th European Turbo-Machinery Conference, 24-28th April 2023, Budapest, Hungry.

[31] A.S. Abdeldayem, M.T. White, A. Paggini, M. Ruggiero, A.I. Sayma, Integrated aerodynamic and structural blade shape optimization of axial turbines operating with supercritical carbon dioxide blended with dopants, J. Eng. Gas Turbines Power 144 (10) (2022) http://dx.doi.org/10.1115/1.4055232.

[32] M.V. Petrovic, W. Riess, Off-design flow analysis and performance prediction of axial turbines, in: Proceedings of the ASME Turbo Expo, June 2–5, 1997, Orlando, Florida, USA.

[33] S.I. Salah, M.T. White, A.I. Sayma, A comparison of axial turbine loss models for air, sCO$_2$ and ORC turbines across a range of scales, Int. J. Thermofluids (2022) 100156, http://dx.doi.org/10.1016/j.ijft.2022.100156.

[34] A.S. Abdeldayem, S.I. Salah, O. Aqel, M.T. White, A.I. Sayma, Design of a 130 MW axial turbine operating with a supercritical carbon dioxide mixture for the SCARABEUS project, in: 15th European Turbo-Machinery Conference, 2023.

[35] R.F. Martins, C.M. Branco, A.M. Gonçalves-Coelho, E.C. Gomes, Metallurgical study of a AISI 316L stainless steel used in a gas turbine exhaust system, in: Materials Science Forum, Vol. 514, Trans Tech Publ, 2006, pp. 1521–1525.

[36] G. Manzolini, M. Binotti, D. Bonalumi, C. Invernizzi, P. Iora, CO$_2$ mixtures as innovative working fluid in power cycles applied to solar plants. Techno-economic assessment, Sol. Energy 181 (2019) 530–544.